# Vanished evaporites, halokinetic structure, and Zn-Pb mineralization in the world-class Angouran deposit, northwestern Iran

Liangliang Zhuang[1], Yucai Song[1,†], David Leach[2], Yingchao Liu[1], Zengqian Hou[1], and Mahmood Fard[3]

[1]*Key Laboratory of Deep-Earth Dynamics, Institute of Geology, Chinese Academy of Geological Sciences, Beijing 100037, China*
[2]*Department of Geology and Geological Engineering, Colorado School of Mines, 1516 Illinois Street, Golden, Colorado 80401, USA*
[3]*Tarbiat Modares University, Tehran 14115-175, Iran*

## ABSTRACT

The Angouran deposit (19.3 Mt at 23.4% Zn and 4% Pb) is the second-largest Zn-Pb deposit in Iran. The deposit is hosted in a Neoproterozoic–Cambrian marble-schist sequence within a breccia pipe in a domal structure, with sulfide mineralization under low-temperature hydrothermal conditions (<200 °C). The features of the ore-hosting breccias are similar to known halokinetic diapir breccias in the world but evaporite minerals are subtle. The common types of breccia clasts in the Angouran breccia pipe include a matrix-supported angular clast (float breccia) with highly variable sizes and orientations and exotic volcanic clasts. The volcanic clasts were derived from the underlying Miocene volcanic rocks, evidenced by the consistent petrography and zircon U-Pb ages dated at 20–19 Ma. Abundant smithsonite pseudomorphs after anhydrite and anhydrite inclusions within sphalerite and pre-ore marcasite in the breccia matrix indicate that the breccia pipe contains abundant anhydrite prior to the Zn-Pb mineralization. The enrichment of evaporite is also supported by the occurrence of considerable double-terminated quartz crystals that contain spherical and tabular carbonate inclusions and anomalously high Li, Na, and K concentrations, relatively high B concentration, and high $\delta^{18}O$ values (up to 28.3‰). These observations suggest the Angouran deposit formed in a former halokinetic diapir breccia pipe. The halokinetic diapirism was possibly triggered by thrust loading of the marble-schist sequence over the Miocene evaporite beds during the Arabia-Eurasia continental collision. Halokinetic structures elsewhere in the Angouran region warrant this consideration. Most of the evaporite minerals in the breccia pipe were dissolved and replaced before and/or during subsequent Zn-Pb sulfide and smithsonite mineralization events. This study provides a good example for the identification of vanished evaporites, halokinetic structure, and associated Mississippi Valley-type mineralization.

## INTRODUCTION

Evaporite diapirs and related halokinetic structures have been widely accepted as excellent exploration targets for oil and gas in salt basins (Hudec and Jackson, 2007; Warren, 2016; Jackson and Hudec, 2017). Numerous recent studies have highlighted the importance of halokinetic structures in controlling Mississippi Valley-type (MVT) Zn-Pb ores, which are one of the world's most important sources of zinc and lead (Warren, 2016; Bouhlel et al., 2016; Leach et al., 2017; Perona et al., 2018; Leach and Song, 2019; de Oliveira et al., 2019; Rddad et al., 2019; Song et al., 2020; Rosa et al., 2022). These halokinetic structures commonly contain abundant evaporite minerals and are thus relatively easily identified. However, direct evidence for the recognition of halokinetic structures can be problematic when evaporite minerals are removed from the rock records by dissolution and/or alteration to other minerals during burial or hydrothermal processes (e.g., Ruan et al., 1991; Jackson et al., 2003; Hitzman et al., 2012; Hearon et al., 2015; Warren, 2016; Leach and Song, 2019). In this case, the identification of halokinetic structure with minor or without evaporites is crucial for the establishment of its relationship with MVT Zn-Pb mineralization.

This study discusses the genesis of the ore-hosting breccia pipe in the Angouran deposit of northwestern Iran, which may provide a good example for the recognition of vanished evaporites, halokinetic structure, and associated MVT mineralization. The Angouran deposit contains 4.7 Mt of sulfide ore with 27.7% Zn, 2.4% Pb, and 110 g/t Ag, and 14.6 Mt carbonate ore with 22% Zn and 4.6% Pb (Gilg et al., 2006). The high-grade sulfide ores are described as a product of low-temperature (<200 °C) mineralization systems (Gilg et al., 2006; Boni et al., 2007; Daliran et al., 2013; Zhuang et al., 2019). A notable feature of the ores is their occurrence within a large discordant breccia pipe hosted in a sequence of metamorphic rocks that are thrusted onto Miocene evaporite-bearing volcanic and sedimentary sequences. Previous studies have not adequately addressed the nature of the breccia pipe that clearly sets it apart from other Zn-Pb deposits in the region. Gilg et al. (2006) proposed that the breccia pipe resulted from tectonic or hydraulic fracturing during ore deposition based on the presence of host rock clasts that are supported by sulfides. Daliran et al. (2013) noted the restriction of brecciation to the ores and the hanging wall marble and further attributed the brecciation to overpressured ore fluids. The absence of a clear understanding of the breccia pipe and its role in the genesis of the Angouran ore system limits exploration for similar deposits in the region.

The salient feature of the Angouran breccia pipe is the presence of exotic clasts of volcanic rocks in addition to the wall-rock clasts (marble and schist). This observation is difficult to explain by tectonic or hydraulic fracturing or volcanism considering the lack of evidence for high-temperature hydrothermal alterations. However, this feature is commonly produced during the halokinetic migration of salt in a diapiric environment that can transport rock clasts upward in a diapiric zone (Ruan et al., 1991; Stern et al., 2011; Thomas et al., 2015; Warren, 2016, and references therein). Considering the widespread occurrence of salt tectonic structures in the Angouran region (Fig. 1B; Arian, 2012; Ballato et al., 2017), the role of halokinesis for the Angouran breccia pipe warrants consideration.

To examine the assumption that the Angouran breccia pipe is a result of halokinetic diapirism, this study conducted petrological, geochemical,

Yingchao Liu ⬤ https://orcid.org/0000-0002-5095-9514
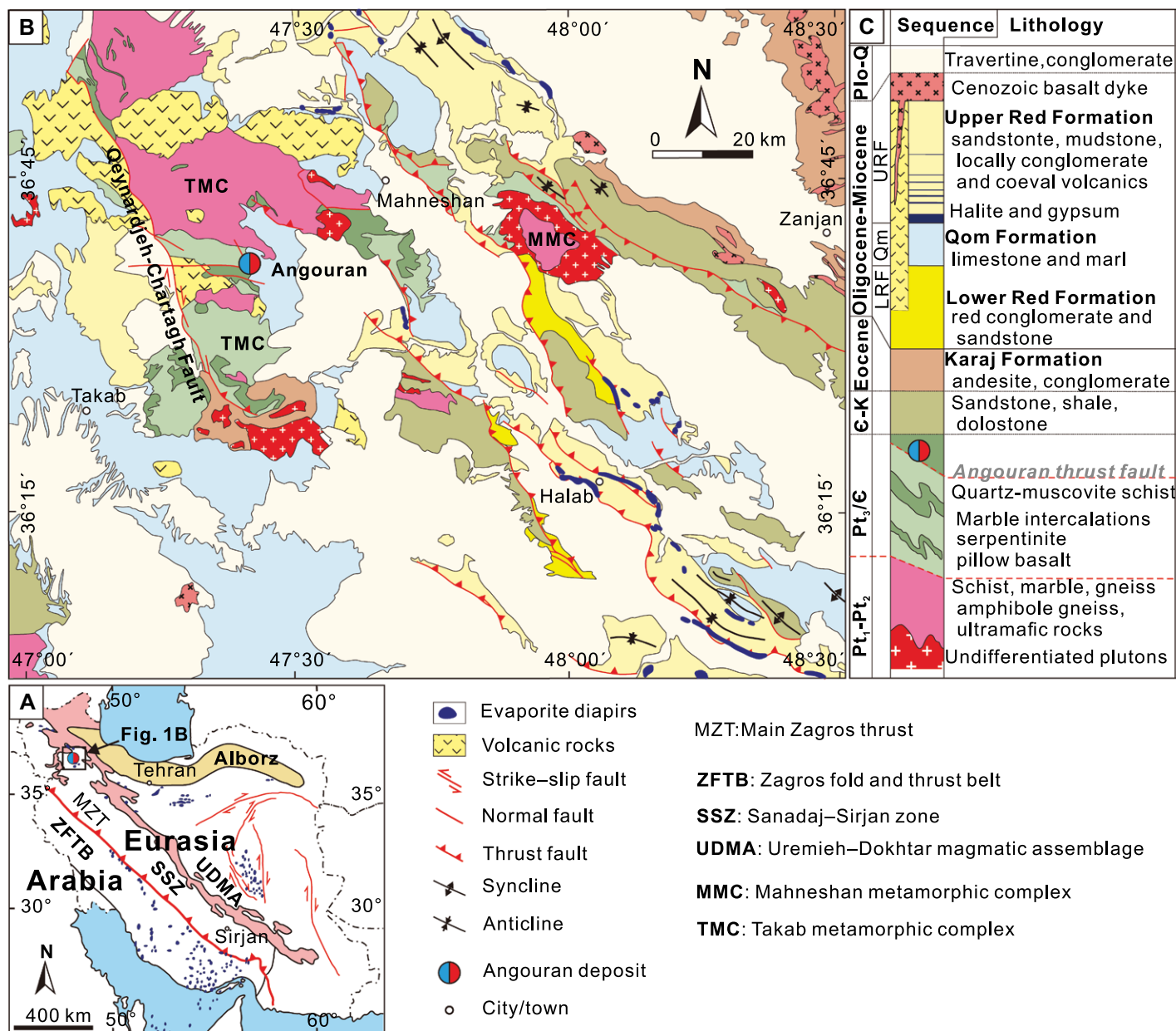†song_yucai@aliyun.com

1569

Figure 1. (A) Geological framework of Iran showing the tectonic divisions and the widespread occurrences of evaporite diapirs in the Zagros fold and thrust belt and the Central Iran Block (modified from Alavi, 1994; Talbot et al., 2009; Agard et al., 2011). (B) Geological map of the Angouran-Zanjan area, northwestern Iran (modified from Stöcklin and Eftekharnezhad, 1969; Alavi and Amidi, 1976; Heidari et al., 2015; Ballato et al., 2017). (C) Generalized stratigraphy columns of the Angouran-Zanjan area (modified from Daliran et al., 2013). LRF—Lower Red Formation; Qm—Qom Formation; URF—Upper Red Formation; Pt$_1$-Pt$_2$—Paleoproterozoic–Mesoproterozoic; Є—Cambrian; K—Cretaceous; Plo—Pleistocene; Q—Quaternary.

and geochronological investigations of the ore-hosting breccias. Petrography and geochronology of the volcanic clasts from the sulfide ores within the breccia pipe are compared to those of the regional Miocene volcanic rocks, aiming to reveal the source of the volcanic clasts; the breccia matrix is petrographically checked to identify the possible presence of (former) evaporite minerals; trace elements and oxygen isotope in quartz with double-terminated crys-tals in the breccia matrix are analyzed in situ to check the relationship between the unusual quartz and evaporative environments; sulfur isotopes of sphalerite and marcasite are analyzed in situ to help the reconstruction of the paragenetic sequence for the brecciation and mineral history. All these observations and data, mostly focus-ing on the identification of vanished evaporites, allow us to interpret the genesis of the breccia pipe and establish the relationship between halo-kinetic diapirism and MVT Zn-Pb mineraliza-tion in the Angouran deposit.

## GEOLOGIC AND TECTONIC SETTING

The Angouran deposit is located in the north-western part of the Sanandaj-Sirjan zone (SSZ), a tectonic belt that is over 1500 km long and 150–200 km wide, within the Zagros orogen of Iran (Fig. 1A; Alavi, 1994). The SSZ is bounded

by the Main Zagros Thrust Fault to the southwest and the Urumieh-Dokahtar Magmatic Arc to the northeast (Fig. 1A). It was the active southwest margin of the Central Iran Block (CIB) during the northeastward subduction of the Neo-Tethyan oceanic plate in the Late Triassic to Late Cretaceous (Agard et al., 2005; Ghasemi and Talbot, 2006; Chiu et al., 2013; Hassanzadeh and Wernicke, 2016). The timing of the initial continental collision between the Arabian and Eurasian plates is controversial, but most studies have suggested that collision began at ca. 27–25 Ma (Fig. 1A; Mouthereau et al., 2012; McQuarrie and van Hinsbergen, 2013; Hassanzadeh and Wernicke, 2016; Koshnaw et al., 2019). Foreland basins in the CIB and northwestern SSZ were formed since the Miocene (ca. 20 Ma) (Talbot and Aftabi, 2004; Ballato et al., 2008, 2011, 2017; Nadimi and Nadimi, 2008; Morley et al., 2009).

Angouran lies in the Zanjan area in the northwestern SSZ. The Precambrian Takab metamorphic complex is exposed at the western and southwestern margins of this area and forms the basement of the Cenozoic Great Pari Basin (Moazzen et al., 2009; Ballato et al., 2017). The metamorphic rocks are greenschist to amphibolite facies and include interlayered mafic granulite, granitic gneiss, amphibolite, migmatite, pelitic schist, meta-ultramafic rock, and calc-silicate rock (Figs. 1B and 1C). These rocks may represent remnants of the Proto-Tethys oceanic lithosphere and Cadomain magmatic arc (ca. 562–505 Ma; Hassanzadeh et al., 2008; Saki, 2010; Moghadam et al., 2017; Honarmand et al., 2018) and have experienced intense rapid uplifting and exhumation during the early Miocene (ca. 20 Ma; Mehrabi et al., 1999; Stockli et al., 2004; Gilg et al., 2006; Ballato et al., 2017). Minor Cambrian–Eocene weak metamorphic sandstone and dolostone are locally present in the area (Fig. 1B). The early stage of the Cenozoic basin in this area was thought to be formed in an extensional interarc setting (Stockli et al., 2004; Gilg et al., 2006; Alizadeh, 2017) and contains Eocene andesitic lava and conglomerate of the Karaj Formation, early Oligocene terrestrial siliciclastic, volcaniclastic, and volcanic rocks of the Lower Red Formation (LRF), and late Oligocene to early Miocene shallow marine limestones and fossiliferous marls of the Qom Formation (Figs. 1B and 1C; Rahimpour-Bonab and Kalantarzadeh, 2005; Alireza et al., 2007). The late stage of the Cenozoic basin was thought of as an asymmetric foreland basin, filled with middle to late Miocene (<ca. 20 Ma) terrestrial red beds and evaporites of the Upper Red Formation (URF) and coeval volcanic and volcaniclastic rocks (e.g., Rahimpour-Bonab and Kalantarzadeh, 2005; Reuter et al., 2009; Ballato et al., 2017). Evaporite horizons, consisting mainly of potassic salts, halite, and gypsum/anhy-

drite with a thickness over 200 m, are exclusively present in the basal part of the URF (Fig. 1C; Rahimpour-Bonab and Kalantarzadeh, 2005; Alizadeh, 2017). The volcanic rocks within the LRF to the URF are andesitic to acidic, late Oligocene–middle Miocene (ca. 25–15 Ma) in age, and mainly distributed at the western and northern margins of the Cenozoic basin.

Thrust and dextral transpressional faults and halokinetic features are the main structural styles in the Angouran-Zanjan area (Fig. 1B; Allen et al., 2011; Arian, 2012; Ballato et al., 2017). The NNW-trending Geynardjeh-Charhartagh fault is a dextral strike-slip fault that records >15 km of displacement (Allen et al., 2011). The basement rocks are thrusted over Cenozoic volcanic and sedimentary rocks along NW-trending faults (Fig. 1B; Daliran et al., 2013; Ballato et al., 2017). Some of the evaporites within the basal URF have reached the surface as diapiric evaporite sheets alongside NW-SE–trending thrust faults in the Mahneshan-Halab area, several tens of kilometers east of the Angouran mine (Fig. 1B; Rahimpour-Bonab and Kalantarzadeh, 2005; Arian, 2012; Ballato et al., 2017), suggesting that the evaporite halokinesis is associated with the oblique collision between the Arabian and Eurasian plates (Fig. 1B; Arian, 2012).

## GENERAL FEATURES OF THE ANGOURAN DEPOSIT

The Angouran deposit is hosted within a discordant breccia pipe in a Neoproterozoic–Cambrian metamorphic sequence that comprises the upper unit of calcitic marble and the lower unit of quartz-sericite, muscovite, and biotite schists. The ore-hosting sequence with minor ultramafic rocks are thrusted over the Qom Formation limestones and marls and the URF volcanic and volcaniclastic rocks (Figs. 2A and 2C). The ore zone appears as a domal structure within the marble-schist sequence (Fig. 2A). Both Zn and Pb sulfide and carbonate mineralization occur in a discordant breccia pipe that is bound by high-angle faults (Fig. 2D). The breccia zone extends from the marble-schist boundary to the interior of the marble unit, and has a diameter of 200–400 m and a depth greater than 200 m (Fig. 2D).

Sulfide ores, mainly sphalerite with subordinate galena, occur in the breccia matrix located in the bottom part of the breccia pipe, near the boundary between the marble and schist units (Fig. 2D). Anhydrite occurs in the sphalerite as mineral inclusions and trace amounts of marcasite and pyrite are present in the breccia matrix. The middle and upper parts of the breccia pipe are dominated by carbonate ores, although sulfide ores occur locally. Mixed sulfide-carbonate ores occur between the zones of discrete sulfide and

carbonate ores. Carbonate ores consist mainly of smithsonite, with minor sulfides, hemimorphite, cerussite, and Fe-Mn oxides in breccias or veins (Gilg et al., 2006; Boni et al., 2007; Daliran et al., 2013; Zhuang et al., 2019). Double-terminated quartz is common in sulfide and carbonate ores.

## SAMPLES AND METHODOLOGY

### Petrography

Nearly 100 samples were collected from the Angouran open pit and underground. Most of them are breccias that contain sulfides and/or Zn carbonates. These samples were made into 30 μm thick, polished thin sections for microscopic observation. Back-scattered electron, cathodoluminescence (CL), and element mapping images were obtained using an FEI Nova Nanosem-450 scanning electron microscope equipped with a backscatter electron detector and energy-dispersive spectrometer under 20 kV accelerating voltage, 20 nA beam current with a working distance of ~15 mm at the Institute of Geology, Chinese Academy of Geological Science (CAGS), Beijing, China.

### Laser Raman Probe Analyses

Laser Raman Probe analyses were conducted to identify minerals with a Renishaw 2000 laser Raman spectrometer at the Key Laboratory of Metallogeny and Mineral Assessment, Institute of Mineral Resources, CAGS. The Ar$^+$ laser excitation wavelength was 514.5 nm, the diameter of the laser beam was 1 μm, and the laser power at the sample surface was 20 mW, with a 1 cm$^{-1}$ spectrometer and the scanning range between 100 cm$^{-1}$ and 1500 cm$^{-1}$. The spectrum was calibrated with silica with an accuracy of ±0.2 cm$^{-1}$. Typical Raman spectra of anhydrite, quartz, sphalerite, and carbonate minerals are shown in Figure S1[1].

---

[1]Supplemental Material. Figure S1: (A) Raman spectra of anhydrite and dolomite inclusions in S1 sphalerite; (B) Raman spectra of dolomite and spherical calcite inclusions in double-terminated quartz; (C) Raman spectra of tabular dolomite inclusion and the host double-terminated quartz. Figure S2: Concentrations of Li, Na, and K versus Al of the double-terminated quartz at Angouran. Table S1: U-Pb data of zircons from Miocene tuffaceous pyroclastic rocks and volcanic clasts-bearing breccias in the Angouran deposit. Table S2: Sulfur isotope composition of sulfides in the Angouran deposit. Table S3: Quantitative LA-ICP-MS trace element data of double-terminated quartz in the Angouran deposit (concentrations in ppm). Table S4: Oxygen isotope composition of quartz from the sulfide ores and footwall schist in the Angouran deposit. Please visit https://doi.org/10.1130/GSAB.S.23154341 to access the supplemental material, and contact editing@ geosociety.org with any questions.
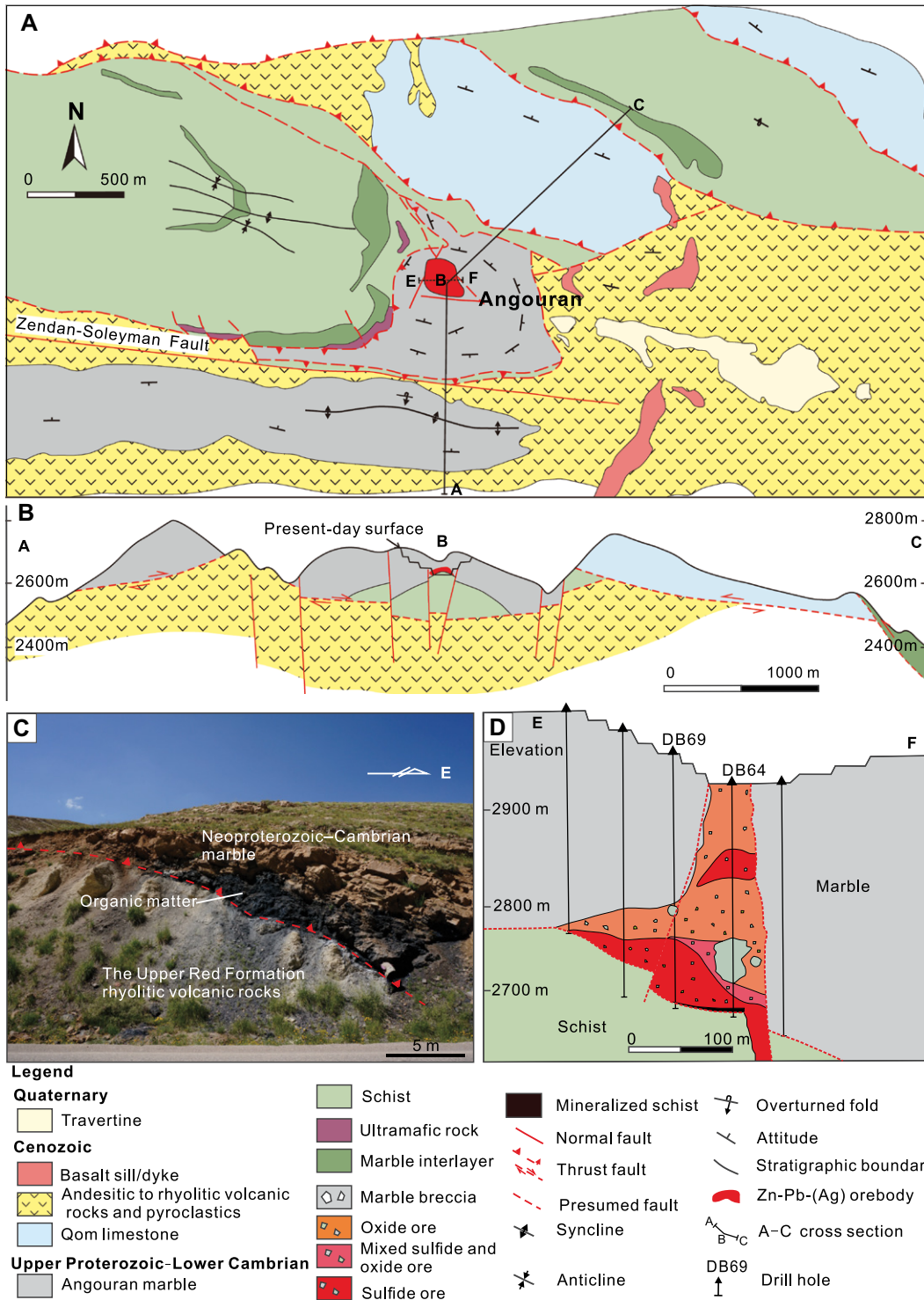
**Figure 2. (A) Geological map of the Angouran mine in northwestern Iran (modified from Daliran et al., 2013). (B) A–B–C cross section showing that the Neoproterozoic–Cambrian marble-schist sequence was thrust onto the Oligocene–Miocene sedimentary and volcanic rocks (modified from Daliran et al., 2009). (C) Photograph shows the Neoproterozoic–Cambrian marble thrust onto the Miocene tuffaceous rocks, southwest of the Angouran open pits. (D) E-W–trending cross section showing the sulfide and nonsulfide mineralization in a discordant breccia pipe (modified from Boni et al., 2007).**

## Zircon Separation and U-Pb Dating

Miocene tuffaceous pyroclastic rocks were sampled (AN13-22-1) from ~500 m south of the Angouran open pit. Volcanic clasts-bearing breccias were sampled (AN14-7-9, AN14-7-11) from the Angouran open pit. Notably, the two samples also contain abundant schist clasts.

Zircon separations for the sample AN13-22-1 and the other two samples were undertaken at two different labs to avoid contamination during the sample treatment. After conventional heavy liquid and magnetic separation, zircon crystals were handpicked under a binocular microscope and then mounted in an epoxy resin and polished to expose the surface. Cathodolumines-

cence imaging and U-Pb dating of the zircons were conducted at SHRIMP Center, CAGS. A high-resolution ion microprobe (SHRIMP) was used to measure the U-Pb isotope. Detailed analytical procedures refer to Williams (1998). The analysis has a mass resolution of ~5000 (1% definition) and the intensity of the primary $O_2^-$ ion beam at 4–6 nA with the spot size of

25 μm. Each spot was rastered for 180 s prior to analysis and five scans through the mass stations were conducted for each age determination. The TEMORA zircons ($^{206}Pb/^{238}U$ age = 417 Ma) were used as standards (Williams, 1998; Black et al., 2003). Data were processed with the Excel-based Squid and Isoplot programs, common lead was corrected by the measured $^{204}Pb$, and weighted mean ages of individual samples are quoted at the 95% confidence level ($2\sigma$) (Ludwig, 2003). Results are given in Table S1.

## Sulfur Isotope Analysis

In situ sulfur isotope analyses of marcasite, sphalerite, and galena were conducted at the State Key Laboratory of Continental Dynamics, Northwest University, Xi'an, China. The Nu Plasma 1700 multicollector inductively coupled plasma–mass spectrometer (ICP-MS) system is equipped with 16 Faraday cups and three ion counters and connected to a Resolution M-50 (ASI) 193-nm ArF Excimer laser ablation system. This system was able to completely separate any interference peaks for $^{32}S$ and $^{33}S$ in medium and a higher resolution mode, respectively (Bao et al., 2017; Chen et al., 2017). Helium gas (gas flow = 280 mL min$^{-1}$) was used as a carrier gas during the laser ablation process. Single-spot ablation has a spatial resolution of 30 μm with a fluence of 3.5 J/cm$^2$ and laser frequency of 4 Hz. Each scan consisted of a 30 s background measurement, an additional 50 s ablation and data collection, and 120 s wash time. The external bracketing standards for sulfur isotope analysis are comprised of NBS123 ($\delta^{34}S_{V\text{-CDT}}$ = 17.8‰ ± 0.2‰) and PTST3 ($\delta^{34}S_{V\text{-CDT}}$ = 26.4‰ ± 0.3‰) for sphalerite, Py-4 ($\delta^{34}S_{V\text{-CDT}}$ = 1.7‰ ± 0.3‰) for marcasite, and CBI-3 ($\delta^{34}S_{V\text{-CDT}}$ = 28.5‰ ± 0.4‰) for galena (V-CDT—Vienna-Canyon Diablo Troilite). Detailed analytical conditions and data calibration processes were described by Bao et al. (2017) and Chen et al. (2017). Data are listed in Table S2.

## Quartz Laser Ablation (LA)-ICP-MS Trace Elements Analysis

Double-terminated quartz grains were obtained from two sulfide ore samples (AN13-26-4, AN13-36-8) by standard crushing, sieving, heavy liquid, magnetic separation, and handpicking under a binocular microscope. More than 200 quartz grains were mounted in epoxy blocks and then polished. After CL imaging, trace element analyses were conducted on a Thermo iCAP-RQ quadrupole ICP-MS with a Teledyne Analyte G2 193 nm ArF Excimer laser ablation system at the Kevin Stark Research Cen-

ter, James Cook University, Australia. All instrument tuning was performed at a 7 Hz repetition rate, a beam diameter of 35–55 μm, and a laser energy density of 7 J/cm$^2$. The first 30 s was for gas blank measurement and the following 40 s was for sample ablation. NIST 612, NIST 610, GSD-1G, and GSE-1G were used as the primary and secondary standards. The inclusion-free area in the quartz grains was chosen for analysis. The analytical elements include $^7Li$, $^9Be$, $^{11}B$, $^{23}Na$, $^{24}Mg$, $^{27}Al$, $^{29}Si$, $^{31}P$, $^{39}K$, $^{43}Ca$, $^{48}Ti$, $^{55}Mn$, $^{57}Fe$, $^{66}Zn$, $^{71}Ga$, $^{74}Ge$, $^{75}As$, $^{85}Rb$, $^{88}Sr$, $^{93}Nb$, $^{118}Sn$, $^{137}Ba$, and $^{208}Pb$. The contamination of carbonate mineral or fluid inclusion was filtered or discarded by selecting the flat time-resolved laser traces of the spot analyses. Data are given in Table S3.

## Oxygen Isotope Analysis

More than 200 double-terminated quartz grains handpicked from the breccia matrix were mounted in epoxy blocks and then polished. The wall-rock schist samples containing quartz were cut to ~3 mm slices from ~80 μm thick, polished thin sections. The slices were mounted in epoxy blocks and then polished. In situ oxygen isotopes of these samples were analyzed with the SHRIMP IIe/MC at the Beijing SHRIMP Center, CAGS. A primary ion beam of Cs + with a spot size of 25 μm was used. Analytical procedures used are described in Ickert et al. (2008). Data were normalized to the quartz oxygen isotope standard NBS-28 with its recommended Vienna standard mean ocean water (V-SMOW) value of 9.6‰. The analytical uncertainty for NBS-28 was 0.5‰. Results are presented in Table S4.

## RESULTS

### Petrography of Ore-Hosting Breccias

The Angouran breccia consists of rock clasts supported by a matrix of mainly sphalerite and/or smithsonite (Figs. 3 and 4). The breccia clasts are mainly marble and schist from the country rocks with exotic volcanic rock clasts (Figs. 3–5). The breccia clasts vary in diameter from several centimeters to several tens of meters (Figs. 3A and 3B). Both schist and marble clasts are common in the lower marble unit (Figs. 3A and 3B). Breccia clasts are commonly angular, randomly orientated, poorly sorted, and matrix-supported (float breccia) (Figs. 3A–3E). Flow-textured breccias occur locally, comprising a larger clast surrounded by smaller clasts with a preferred orientation (Figs. 3B and 3C) suggestive of migration or ductile flowage of material such as evaporites around brittle clasts. Mosaic breccias contain rock clasts showing some fitting

to adjacent clasts without significant displacement and rotation (Fig. 3D).

The ubiquitous volcanic clasts occur throughout most of the breccia pipe, including crystal tuff, rhyolite, and porphyritic andesite (Figs. 3B, 3E, and 4). Most of the volcanic fragments are variably altered and partly preserve their original volcanic textures (Fig. 4). The crystal tuff contains the phenocrysts of biotite and plagioclase in a matrix of fine-grained quartz (Figs. 4A and 4B). The plagioclase phenocrysts were commonly devitrified to calcite and quartz (Fig. 4B). The rhyolite displays a typical rhyolitic texture and contains vitric pyroclasts and vermiculite (Figs. 4C and 4D). Andesite contains phenocrysts of plagioclase and amphibole/biotite in a devitrified matrix (Figs. 4E and 4F). Chlorite occurs in the phenocrysts and matrix of the andesite (Fig. 4F).

### Breccia Matrix

This study focuses on the breccia matrix in sulfide ores where sulfides are dominated by sphalerite, subordinate galena, and trace amounts of marcasite and pyrite (Figs. 3–6). Smithsonite and double-terminated quartz also occur in the matrix (Figs. 5, 7, and 8). Anhydrite inclusions are identified within sphalerite and marcasite, and dolomite and calcite inclusions commonly occur in the sulfides and quartz (Figs. 7 and 8). The matrix also contains small fragments of schist and marble from the country rocks.

#### *Sphalerite*

Two stages of sphalerite are present: early dark-brown sphalerite (S1) and later honey-yellow sphalerite (S2) (Figs. 3D and 5A–5C). Sphalerite (S1) appears to be co-genetic with S1 galena. Tabular smithsonite (S3) and double-terminated quartz occur within the S1 sphalerite (Figs. 5A, 5C, and 5D). Honey-yellow sphalerite (S2) coexists with S2 galena and occurs as veins or oscillatory-zoned aggregates (Fig. 5B). Some S1 sphalerite occurs as pseudomorphs after anhydrite that has been partially replaced by smithsonite (Figs. 5E and 5F).

#### *Marcasite and Pyrite*

These two minerals are generally low in abundance but locally abundant in the breccia matrix (Fig. 6A). They are commonly broken into small fragments that are cemented by S1 sphalerite (Fig. 3E inset). Marcasite in the breccia matrix displays a radial morphology (Figs. 6B and 6C).

#### *Anhydrite*

Detailed microscopic observations and laser Raman analyses reveal substantial amounts of anhydrite inclusions in S1 sphalerite and marcasite
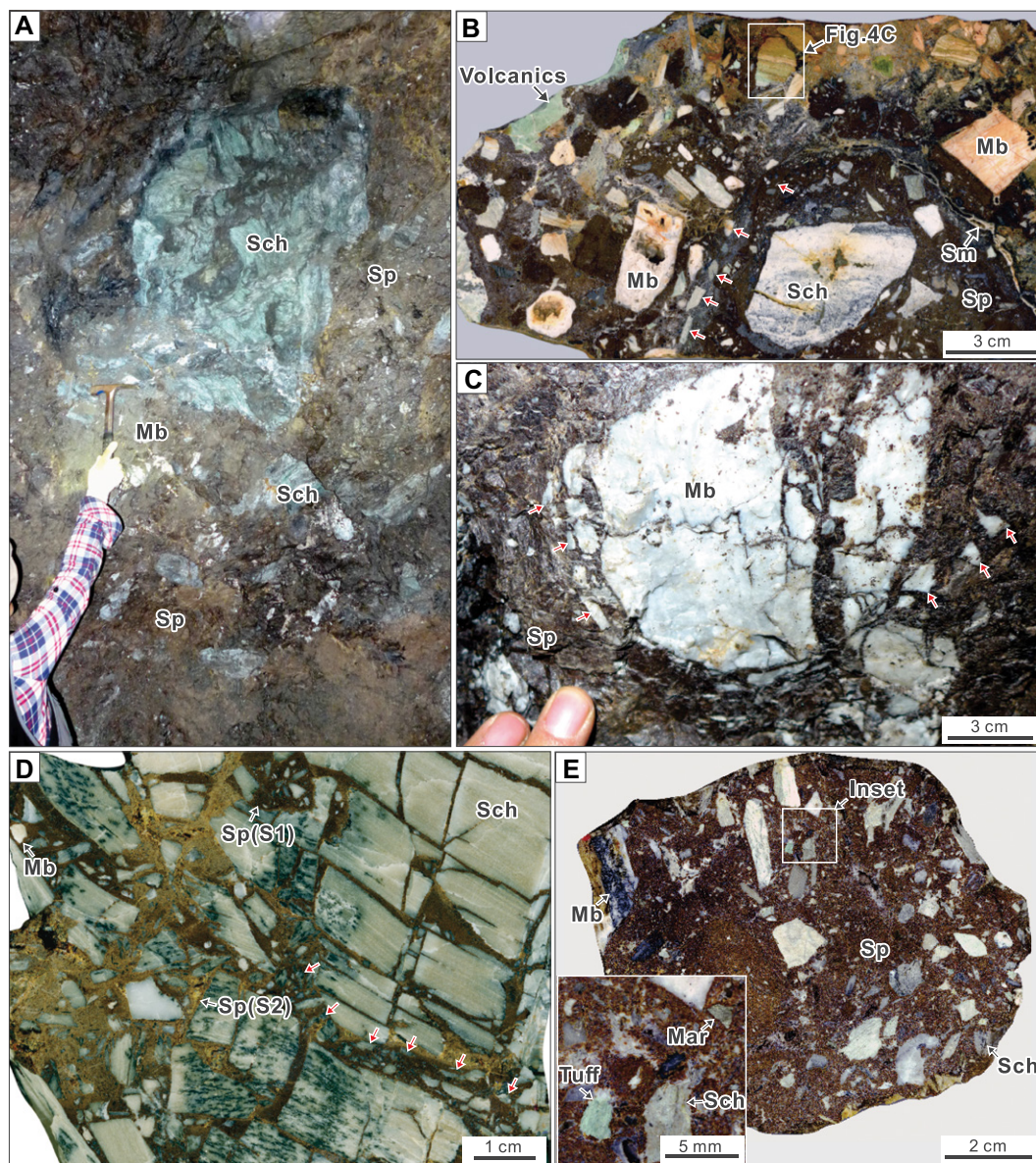
Figure 3. Photographs showing the representative ore-hosting breccias in the Angouran deposit, northwestern Iran. (A) An angular schist megabreccia in a sphalerite-dominated matrix. (B) Clasts of volcanic rocks, marble, and schist in a sphalerite-dominated matrix, locally showing a flow texture (red arrows). (C) A Flow-textured breccia, showing preferentially oriented smaller marble clasts surrounding a larger marble clast in a matrix of sphalerite (red arrow). (D) Two stages of sphalerite mineralization cementing the schist clasts, showing a mosaic and floated texture (red arrows). (E) Clasts of marble and schist in a sphalerite-dominated matrix. Inset shows that marcasite and volcanic rocks are present as clasts. Mar—marcasite; Mb—marble; Sch—schist; Sm—smithsonite; Sp—sphalerite; S1—first stage; S2—second stage.

(Figs. 6A, 6C, and 7; Fig. S1A). No anhydrite has been observed within the breccia clasts or within the wall rocks. Gilg et al. (2006) also identified anhydrite inclusions in sphalerite at Angouran. Individual anhydrite grains are stumpy, tabular, and rectangular in morphology and commonly <120 μm long with a typical aspect ratio of ~1:2 to ~1:6 (Figs. 6C, 7B, 7D, and 7E). The partial replacement of anhydrite by sphalerite produced irregular boundaries between the two minerals (Figs. 7D, 7E, and 7G). Elemental mapping of Fe contents indicates that zoned sphalerite filled open spaces between sulfate crystals (Figs. 7H and 7I). The interstitial and replacement textures suggest that anhydrite formed before sphalerite. In addition, anhydrite occurs as inclusions in the cores of marcasite, indicating that anhydrite formed before marcasite (Fig. 6C).

**Smithsonite**

Smithsonite (S3) in the breccia matrix from sulfide ores commonly replaced sphalerite and has tabular and rectangular shapes or irregular aggregates (Figs. 5A–5D). Abundant tabular smithsonite occurs as pseudomorphs after anhydrite (Figs. 5D–5F) and locally has a preferred orientation (i.e., flow textures) (Fig. 5C). The tabular smithsonite is suggested to have been formed as a direct replacement of sphalerite pseudomorphs after anhydrite or infilling tabular cavities created by the dissolution of anhydrite (Figs. 5E, 5F, and 8B). The dissolution and infilling textures were also observed by Boni et al. (2007). The S1 sphalerite filled open spaces between tabular smithsonite crystals (former anhydrite), consistent with the formation of anhydrite before sphalerite (Figs. 5E, 5F, 7H, and 7I).

**Double-Terminated Quartz**

The quartz is ubiquitous in the breccia matrix and exclusively and unevenly distributed within S1 sphalerite (Fig. 8; Gilg et al., 2006; Daliran et al., 2013). Individual quartz crystals are 50–400 μm long and 20–100 μm wide. The quartz grains typically do not physically touch with each other and lack preferential orientation (Figs. 8A and 8B). They can be coeval with anhydrite or anhydrite pseudomorphs at a millimeter scale (Figs. 8B and 8C). Euhedral quartz grains growing from the schist breccia clasts show single-terminated crystals (Fig. 8D). Laser Raman analyses indicate that the double-terminated quartz contains abundant spherical or tabular dolomite and calcite inclusions (Figs. 8D–8F; Figs. S1B and S1C). Some of the double-terminated quartz grains
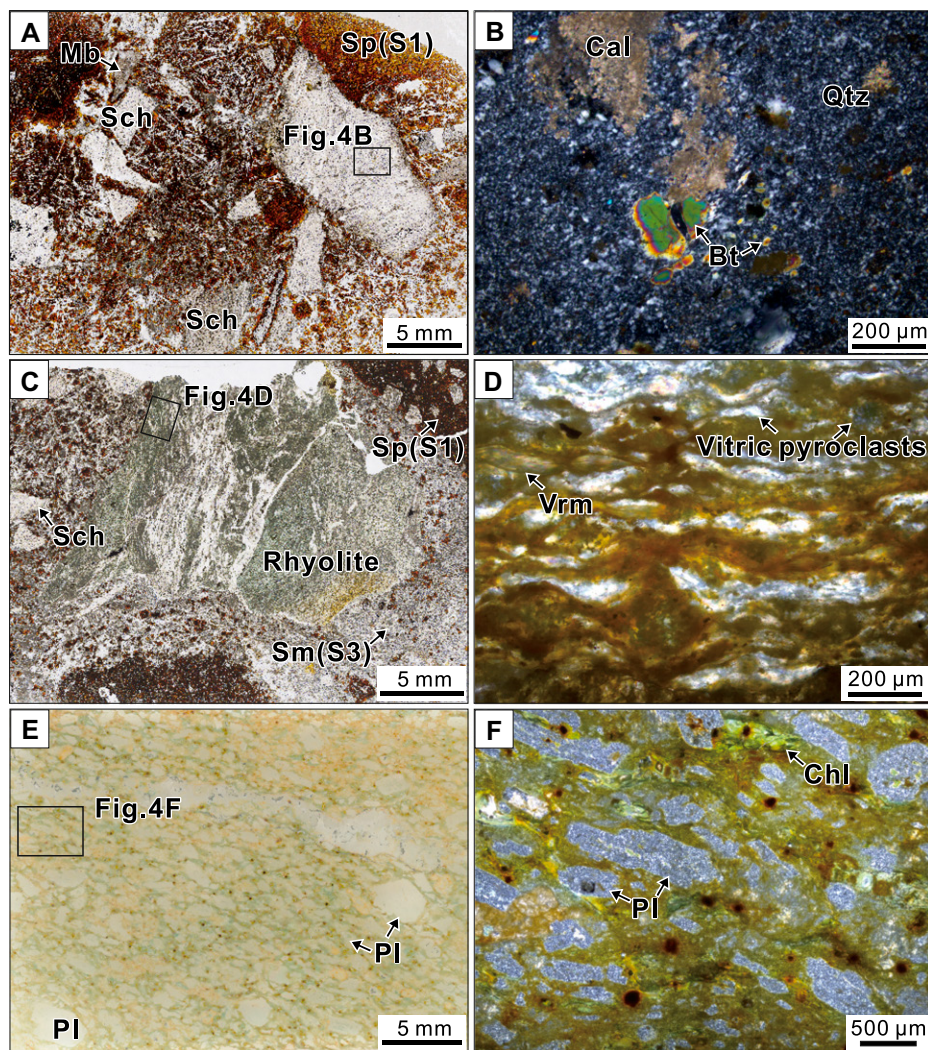
**Figure 4. Photographs and photomicrographs showing volcanic rock clasts in the ore-hosting breccia in the Angouran deposit, northwestern Iran. (A) Scanned thin section of a tuff clast in the matrix of S1 sphalerite and S3 smithsonite. (B) Photomicrograph in cross-polarized light showing the broken biotite phenocryst and the plagioclase phenocryst has totally altered to calcite and quartz. (C) Scanned thin section of a greyish-green vitric rhyolite clast in the matrix of S1 sphalerite and S3 smithsonite. (D) Photomicrograph in cross-polarized showing the typical devitrified rhyolitic texture. Note the spherical and wormlike devitrified vitric pyroclasts. (E) Scanned thin section of an andesite clast from the ore-hosting breccia. (F) Photomicrograph in cross-polarized showing the euhedral plagioclase phenocrysts have completely altered to calcite. Bt—biotite; Cal—calcite; Chl—chlorite; Mb—marble; Pl—plagioclase; Qtz—quartz; Sch—schist; Sm—smithsonite; Sp—sphalerite; Vrm—vermiculite; S1—first stage; S3—third stage.**

have been corroded by sphalerite (Figs. 8D, 8F, and 8G).

## Zircon U-Pb Geochronology

### Miocene Tuffaceous Pyroclastic Rock

Most of the zircon grains from the volcanic rocks (AN13-22-1) in the Angouran region are prismatic euhedral or elongate lath-shape and show oscillatory zonation in CL images (Fig. 9H). Thirty-three analyses of zircons yield relatively high Th/U ratios ranging from 0.17 to 1.78 with $^{206}Pb/^{238}U$ ages from 786 Ma to 14.7 Ma (Fig. 9A; Table S1). The dominant age population ranges from 21.0 Ma to 14.7 Ma ($n = 26$; Fig. 9A). Fourteen analyses are concordant with a weighted mean $^{206}Pb/^{238}U$ age of $18.15 \pm 0.18$ Ma (mean

square of weighted deviates [MSWD] = 0.95) (Fig. 9B). This age is consistent with the previously reported age of ca. 18 Ma (Daliran et al., 2009; Heidari et al., 2015; Ballato et al., 2017; Azizi et al., 2021).

### Volcanic Clasts from the Breccias

The 56 analyses of the zircons from the sample AN14-7-9 yield three discrete age populations (Fig. 9C). The oldest age population ranges from 1012.9 Ma to 462.1 Ma ($n = 7$), which derive from stubby zircon or oval cores and are interpreted to be of inherited origin (Fig. 9H). The second age population has relatively homogeneous Th/U values of 0.13–1.91 and yield $^{206}Pb/^{238}U$ age ranging from 96.3 Ma to 79.1 Ma ($n = 23$; Fig. 9C), which were obtained from stumpy euhedral zircons without inherited cores and from the overgrowth mantle of inherited core (Fig. 9H). Fourteen of the 23 analyses are concordant and yield a weighted mean $^{206}Pb/^{238}U$ age of $84.74 \pm 0.67$ Ma (MSWD = 0.66; Fig. 9D). The youngest age population ranges from 21.1 Ma to 17.6 Ma ($n = 24$; Fig. 9C), which derive from prismatic euhedral or elongate lath-shaped zircons (Fig. 9H). Fourteen of the 24 analyses are concordant and yield a weighted mean $^{206}Pb/^{238}U$ age of $19.76 \pm 0.17$ Ma (MSWD = 1.04; Fig. 9E).

The 39 analyses of the zircons from the sample AN14-7-11 yield two main age populations (Fig. 9F). The first age population has the $^{206}Pb/^{238}U$ ages mainly between 88.0 Ma and 80.7 Ma ($n = 29$; Fig. 9F). The zircons are short to long prismatic euhedral in shape (Fig. 9H). Twenty-one of the 29 analyses are concordant and yield a weighted mean $^{206}Pb/^{238}U$ age of $84.67 \pm 0.54$ Ma (MSWD = 0.66; Fig. 9G).

## Sulfur Isotopes

Sulfur isotope compositions range from 7.2‰ to 8.7‰ (average of 7.6‰, $n = 6$) and from 2.0‰ to 6.6‰ (average of 4.8‰, $n = 5$) for S1 sphalerite and S1 galena, respectively (Figs. 5E and 10; Table S2). Sulfur isotope compositions of S2 sphalerite and S2 galena range from 6.4‰ to 8.5‰ (average of 7.1‰, $n = 3$) and from 4.0‰ to 4.4‰ (average of 4.3‰, $n = 3$), respectively. The in situ analytical results are consistent with previous bulk analytical results (Zhuang et al., 2019). Sulfur isotope compositions of marcasite range from −23.8‰ to −15.8‰ (average of −18.9‰, $n = 5$).

## Trace Elements in Double-Terminated Quartz

This study focuses on the elements Al, Ti, Li, Na, K, and B that are used to discuss the genesis
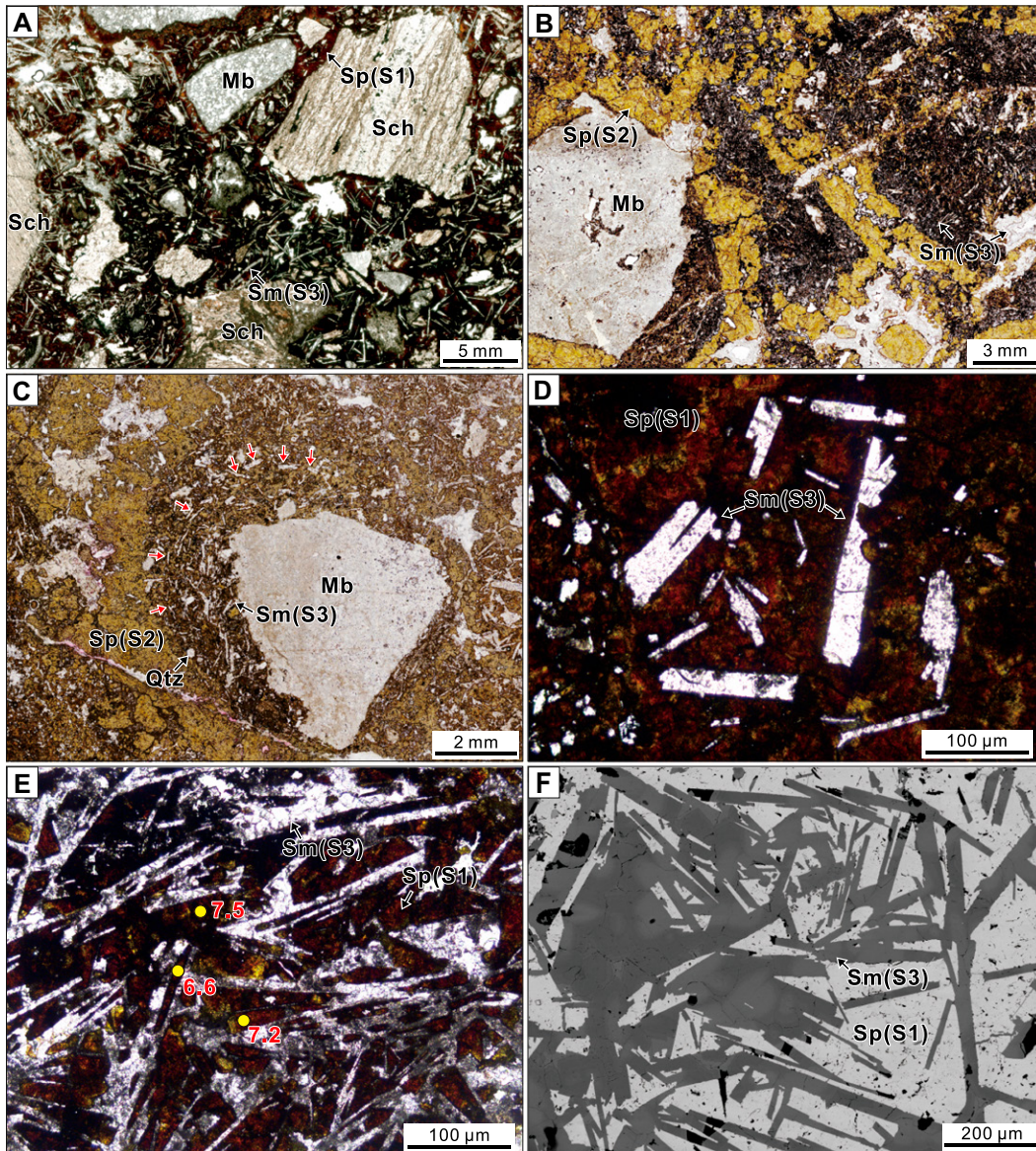
Figure 5. Sphalerite and smithsonite in the breccia matrix in the Angouran deposit, northwestern Iran. Note that sphalerite and smithsonite pseudomorphs after anhydrite are exclusively present in the breccia matrix. (A) Photomicrograph in transmitted light showing dark-brown sphalerite (S1) and tabular smithsonite (S3) as the breccia matrix. (B) Photomicrograph in transmitted light showing that tabular smithsonite exclusively coexists with dark-brown S1 sphalerite, which is rarely associated with honey-yellow sphalerite (S2). Irregular smithsonite aggregates (S3) replaced both stages of sphalerite. (C) Photomicrograph in transmitted light showing a flow-textured breccia consisting of preferentially oriented tabular smithsonite surrounding a larger marble clast in a matrix of sphalerite. (D) Photomicrograph in transmitted light showing the tabular smithsonite pseudomorphs after anhydrite. (E) Photomicrograph in transmitted light showing sphalerite (S1) and smithsonite (S3) pseudomorphs after anhydrite. Sphalerite has been partially or totally replaced by smithsonite. The yellow spots show the position of in situ sulfur isotope analyses with corresponding $\delta^{34}S_{V\text{-}CDT}$ values (‰). (F) Backscattered electron image showing that smithsonite filled the tabular voids with oscillatory zonation. Mb—marble; Qtz—quartz; Sch—schist; Sm—smithsonite; Sp—sphalerite; S1—first stage; S2—second stage; S3—third stage; V-CDT—Vienna-Canyon Diablo Troilite.

of the double-terminated quartz. Titanium and B are commonly thought to occur in the quartz crystal lattice (e.g., Götze et al., 2004; Larsen et al., 2004; Lehmann et al., 2011; Götte, 2018), and Li, Na, K, and Al can substitute Si on a tetrahedral site in quartz crystals (Fig. S2; Landtwing and Pettke, 2005; Götte, 2018).

In situ LA-ICP-MS analysis reveals that Al concentrations in the double-terminated quartz range from 637 ppm to 3668 ppm, with an average value of 2229 ppm, and Ti concentrations range from <1–8 ppm, with an average value of 3 ppm (Fig. 11A; Table S3). Lithium, Na, K, and B concentrations range from 3 ppm to 47 ppm (average of 22 ppm), from 38 ppm to 194 ppm (average of 95 ppm), from 69 ppm to 643 ppm (average of 232 ppm), and from 3 ppm to 47 ppm (average of 15 ppm), respectively. The concentrations of total alkali metal elements (Li + Na + K) range from 110 ppm to 782 ppm (average of 347 ppm; Fig. 11A).

## Oxygen Isotopes of Quartz

Quartz in the schist has homogeneous oxygen isotope compositions, ranging from 24.4‰ to 25.4‰ (n = 11; Fig. 12). In contrast, the double-terminated quartz has variable oxygen isotope compositions, ranging from 20.9‰ to 28.4‰ (n = 33; Fig. 12).

## DISCUSSION

### Origin of the Angouran Breccia

#### *Volcanic Rock Clasts*

The volcanic clasts from the sulfide ores at Angouran include altered crystal tuff, rhyolite, and porphyritic andesite (Fig. 4). Our study and previous studies (Daliran et al., 2013) indicate that these volcanic rock clasts are petrographically identical to the Miocene volcanic rocks in the deposit area. The youngest zircon population from the volcanic clasts-bearing breccias (the sample AN14-7-9) yields a weighted mean $^{206}Pb/^{238}U$ age of 19.76 ± 0.17 Ma (Fig. 9E). The
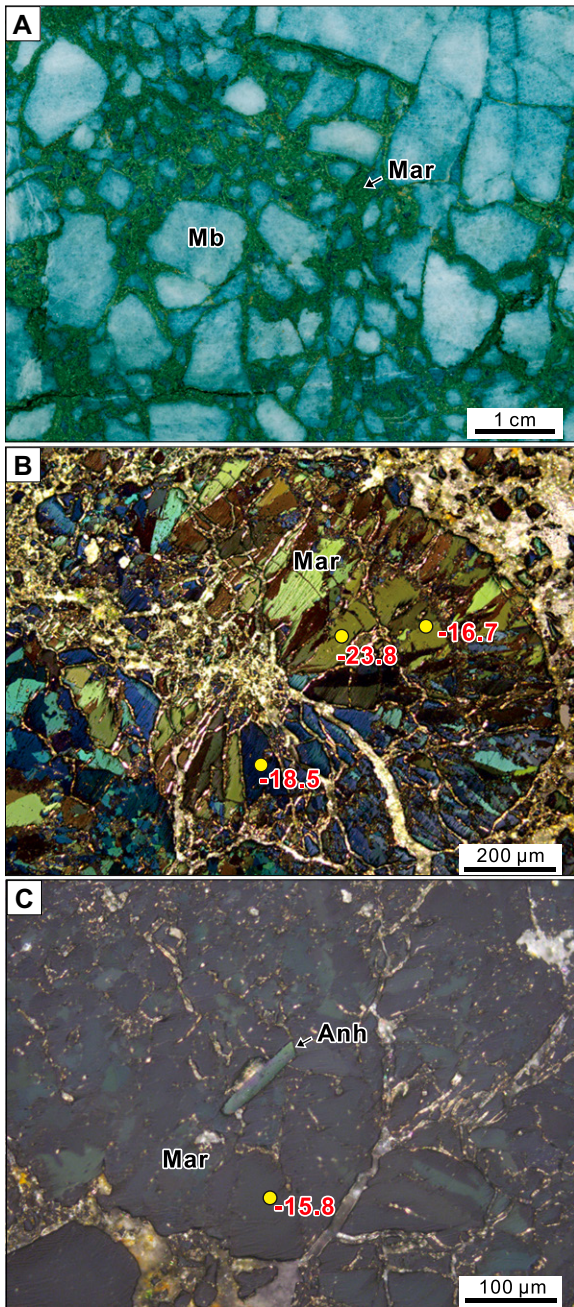
**Figure 6. Marcasite and anhydrite inclusion in the breccia matrix in the Angouran deposit, northwestern Iran. (A) Marble clasts in a marcasite-dominated matrix, showing that marcasite occurs as open-space fillings. (B) Photomicrograph in reflected light showing a rosette-like marcasite crystal. The yellow spots show the location of sulfur isotope analyses with corresponding $\delta^{34}S_{V-CDT}$ values (‰). (C) Photomicrograph in transmitted light showing an anhydrite inclusion in the core of a marcasite crystal. Anh—anhydrite; Mar—marcasite; Mb—marble; V-CDT—Vienna-Canyon Diablo Troilite.**

tion, and epidotization) in the Angouran breccias and adjacent host rocks suggests they are not intrusion-related magmatic-hydrothermal or phreatomagmatic breccias (Ross et al., 2002; Sillitoe, 2010). Sericite and muscovite in the sulfide ores are more likely the relics of the host schists but not a result of the Zn-Pb mineralization alteration because the muscovite gives a $^{40}Ar$-$^{39}Ar$ plateau age of ca. 20 Ma identical to that of unaltered schists that has been interpreted as the cooling age of the basement exhumation and the $^{40}Ar$-$^{39}Ar$ age of sericite in the sulfide ore is disturbed by the Zn-Pb mineralization thermal event (Gilg et al., 2006); the volcanic rock clasts in the ore-hosting breccias have undergone chloritization, but this alteration does not occur in the marble and schist clasts and thus is less likely associated with the Zn-Pb mineralization. The large vertical extent of the breccia pipe containing clasts of exotic volcanic rocks derived from the footwall sequence indicates that the breccias are unlikely to have been generated by carbonate dissolution-collapse processes or tectonic or hydraulic faulting (Sangster, 1988; Jébrak, 1997; Loucks et al., 2004; Woodcock and Mort, 2008). However, upward transportation of rock clasts is common in a diapiric zone (e.g., Warren, 2016; Stern et al., 2011; Thomas et al., 2015; Lawton and Amato, 2017). Evaporites in the Angouran region occur in the basal part of the URF where coeval volcanic rocks have eruption ages of 20–16 Ma (Rahimpour-Bonab and Kalantarzadeh, 2005; Alizadeh, 2017; Ballato et al., 2017). This suggests that the Angouran breccia pipe obtained the Miocene volcanic rock clasts below the deposit by means of the halokinesis of the URF evaporites.

### Anhydrite

Anhydrite inclusions in sphalerite and mineral pseudomorphs after anhydrite are pervasive in the breccia matrix and locally make up ~40% of the matrix by volume (Figs. 5 and 7). Therefore, anhydrite was originally abundant in the breccia matrix. One may argue that the anhydrite is the product of the hydrothermal Zn-Pb mineralization. However, ore-related hydrothermal anhydrite can only be abundant in high-temperature hydrothermal deposits (>250 °C; e.g., porphyry and volcanogenic massive sulfide deposits; Kuhn et al., 2003; Sillitoe, 2010; Warren, 2016; Creaser et al., 2022), as the solubility of anhydrite decreases rapidly with increasing temperature. Ore-related hydrothermal anhydrite is rare in low-temperature (<250 °C) mineralization systems and has only been observed in trace amounts in association with early galena from the Viburnum Trend deposit, USA (Marikos, 1989). At Angouran, anhydrite is unevenly distributed in the sulfide ore and absent in the

zircons also show crystal morphology and CL images consistent with those from the regional Miocene volcanic rocks (Fig. 9H). These suggest that the volcanic rock clasts in the Angouran breccia pipe derived from the Miocene volcanic rocks below the Angouran deposit. Both samples of the volcanic clasts-bearing breccias (AN14-7-9 and AN14-7-11) have zircon populations yielding weighted mean $^{206}Pb/^{238}U$ ages of ca. 85 Ma (Figs. 9D and 9G). However, the regional Miocene volcanic rocks do not contain this age of inherited zircons, and also no ca. 85 Ma volcanic rocks have been reported in the Angouran

region. Therefore, it is less likely that the zircons of ca. 85 Ma are of inherited origin or that they were derived from this age of volcanic rock clasts. As some zircons from the Precambrian greenschist to amphibolite facies rocks in the Angouran region record the metamorphic ages of 95–85 Ma (Daliran et al., 2009), we speculate that the zircons of ca. 85 Ma from the breccia samples were obtained from the schist clasts but not from the volcanic rock clasts during zircon separation and selection.

The absence of typical features of high-temperature hydrothermal alteration (e.g., sericitiza-
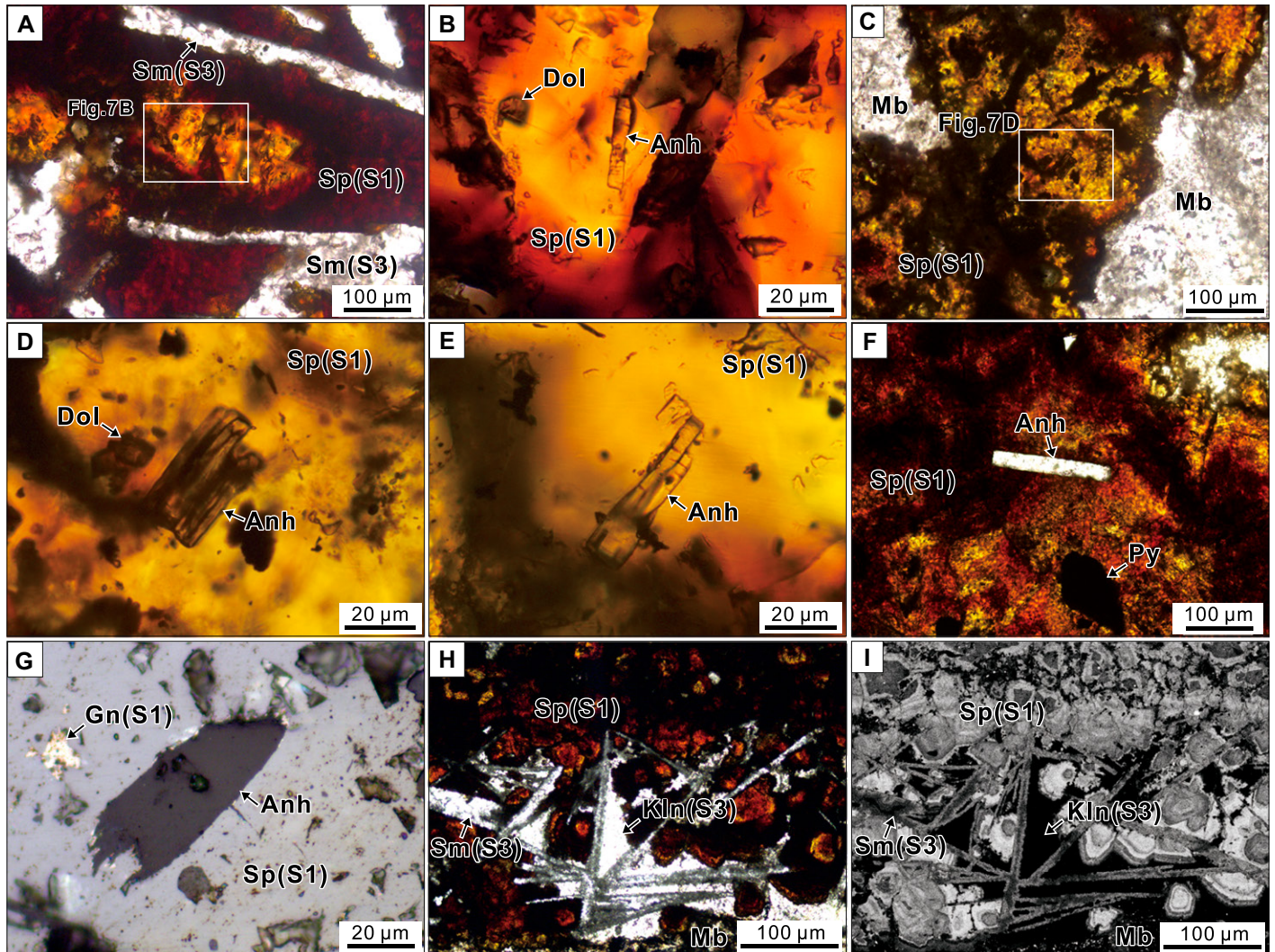
**Figure 7. Anhydrite inclusions in sphalerite from the breccia matrix in the Angouran deposit, northwestern Iran. (A and B) Photomicrographs in transmitted light showing a tabular anhydrite inclusion in S1 sphalerite. (C and D) Photomicrographs in transmitted light showing the coexisting stumpy anhydrite and dolomite rhomb in S1 sphalerite. Note that anhydrite is only present in the breccia matrix. (E) Photomicrograph in transmitted light showing the tabular anhydrite enclosed by S1 sphalerite. (F) Photomicrograph in transmitted light showing a rectangular anhydrite inclusion and a pyrite fragment in S1 sphalerite. (G) Photomicrograph in reflected light showing an anhydrite inclusion with irregular boundaries reflecting the replacement by S1 sphalerite. (H) Photomicrograph in transmitted light showing that S1 sphalerite with oscillatory zonation filled open spaces between tabular smithsonite pseudomorphs after anhydrite. (I) Corresponding photomicrograph of Figure 7H through Fe elemental mapping. Anh—anhydrite; Dol—dolomite; Gn—galena; Kln—kaolinite; Mb—marble; Py—pyrite; Sm—smithsonite; Sp—sphalerite; S1—first stage; S3—third stage.**

marble and schist, inconsistent with the assumption that anhydrite is the product of hydrothermal alteration related to the Zn-Pb mineralization. Gilg et al. (2006) observed that anhydrite formed earlier than Zn and Pb sulfides in the Angouran deposit. Our study shows that the sulfur isotope compositions of marcasite are distinct from those of the two stages of sphalerite and galena (Fig. 10). As the marcasite fragments are cemented by S1 sphalerite, marcasite formed prior to sphalerite and are unlikely to be cogenetic with Zn-Pb mineralization. Anhy-

drite was also entrapped as mineral inclusions within marcasite, so it formed before marcasite and sphalerite and was genetically unrelated to Zn-Pb mineralization. Preferentially oriented tabular smithsonite pseudomorphs after anhydrite surrounding a larger marble clast are characteristic of evaporite flow in a diapiric zone and cannot be the product of the hydrothermal processes. Therefore, we suggest that the pervasive anhydrite at Angouran was part of the mother evaporite that formed the diapir rather than a product of hydrothermal mineralization altera-

tion. Halokinetic tabular anhydrite is well preserved in the Hockley Salt Dome, Texas, USA, and the Winnfield Salt Dome, Louisiana, USA (Price and Kyle, 1983; Price et al., 1983; Kyle and Posey, 1991; Posey et al., 1994; Kyle and Saunders, 1996).

### Double-Terminated Quartz

The quartz is pervasive in the breccia matrix (Fig. 8). Relative to quartz with single-terminated crystals, double-terminated quartz is rare in aqueous hydrothermal systems, as quartz
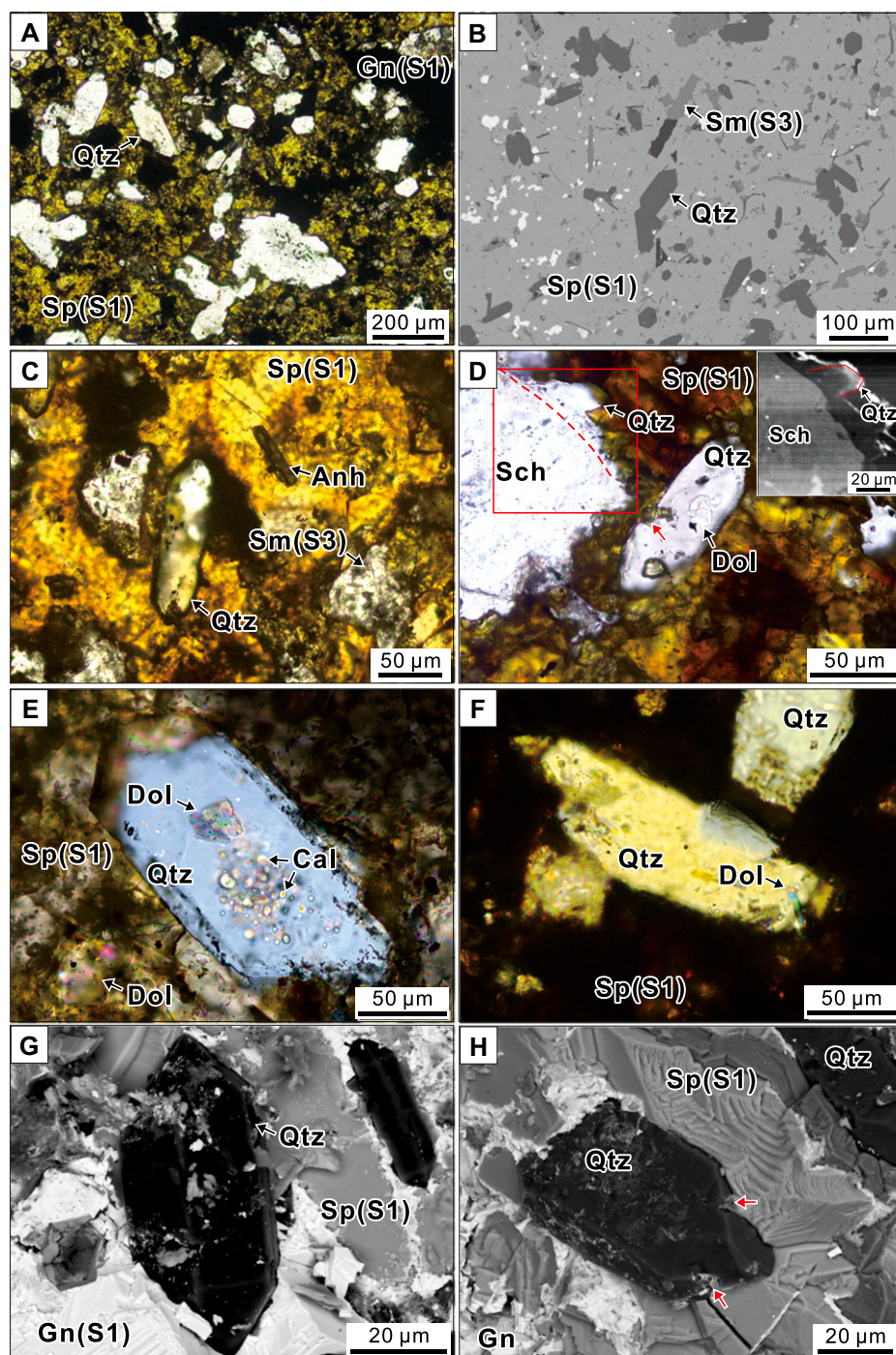
**Figure 8. Double-terminated quartz and carbonate inclusions in the quartz from the breccia matrix in the Angouran deposit, northwestern Iran. (A) Photomicrograph in transmitted light showing double-terminated quartz crystals set in a groundmass of S1 sphalerite. Note that these crystals are distributed haphazardly without any preferred orientation. (B) Backscattered electron image showing the double-terminated quartz set in a groundmass of S1 sphalerite. Note that anhydrite is totally dissolved, leaving the tabular voids partly filled by smithsonite. (C) Photomicrograph in transmitted light showing that both double-terminated quartz and anhydrite occur in S1 sphalerite within a small scale. (D) Photomicrograph in transmitted light showing that euhedral quartz crystallizes on the basis of the schist clasts and double-terminated quartz suspended on the S1 sphalerite. Note that the double-terminated quartz is corroded by S1 sphalerite (red arrow). Inset (cathodoluminescence image) showing that the euhedral quartz deposits on and partly altered the schist breccia. (E) Photomicrograph in transmitted light showing euhedral dolomite and unusual spherical calcite inclusions in a double-terminated quartz crystal. (F) Photomicrograph in transmitted light showing tabular dolomite inclusions in a double-terminated quartz crystal. (G) Scanning electron microscope (SEM) image showing the euhedral quartz crystal embedded in S1 sphalerite with a well-developed face. (H) SEM image showing the double-terminated quartz is corroded by S1 sphalerite. Anh—anhydrite; Cal—calcite; Dol—dolomite; Gn—galena; Qtz—quartz; Sch—schist; Sm—smithsonite; Sp—sphalerite; S1—first stage.**

a matrix of "plastic evaporites" with a density similar to quartz during crystal growth.

The double-terminated quartz at Angouran contains high concentrations of Al and low Ti, suggesting that it precipitated at low temperatures (<350 °C; Figs. 11A and 11B; Rusk et al., 2008; Lehmann et al., 2011). The quartz also has anomalously high Li, Na, and K concentrations and relatively high B concentrations, which are consistent with the compositional signatures of authigenic quartz in hypersaline environments where alkali elements are trapped in the quartz lattice during crystal growth (Figs. 11A and 11C; Lehmann et al., 2011; Götze, 2012). Distinct oxygen isotope compositions indicate that the double-terminated quartz was not derived from the

crystal growth is typically from a surface (e.g., fracture surface or another mineral) into the fluid. Some reports described the occurrence of double-terminated quartz in an aqueous fluid system where extremely high rates of ascending hydrothermal fluids were postulated to have kept the crystals floating and away from any surfaces during the crystal growth (Okamoto and Tsuchiya, 2009). In non-magmatic environments, double-terminated quartz is almost exclusively associated with evaporitic environments, although it has also been found in unconsolidated or semi-consolidated soft sediments (Milliken, 1979; Friedman and Shukla, 1980; Maliva, 1987; Kyle and Posey, 1991; Ulmer-Scholle et al., 1993; Saunders and Swann, 1994; Chafetz and Zhang, 1998; Henchiri et al., 2015; Leitner et al., 2017). The growth of double-terminated quartz is facilitated by the plastic nature of evaporites that allows the crystal to float in
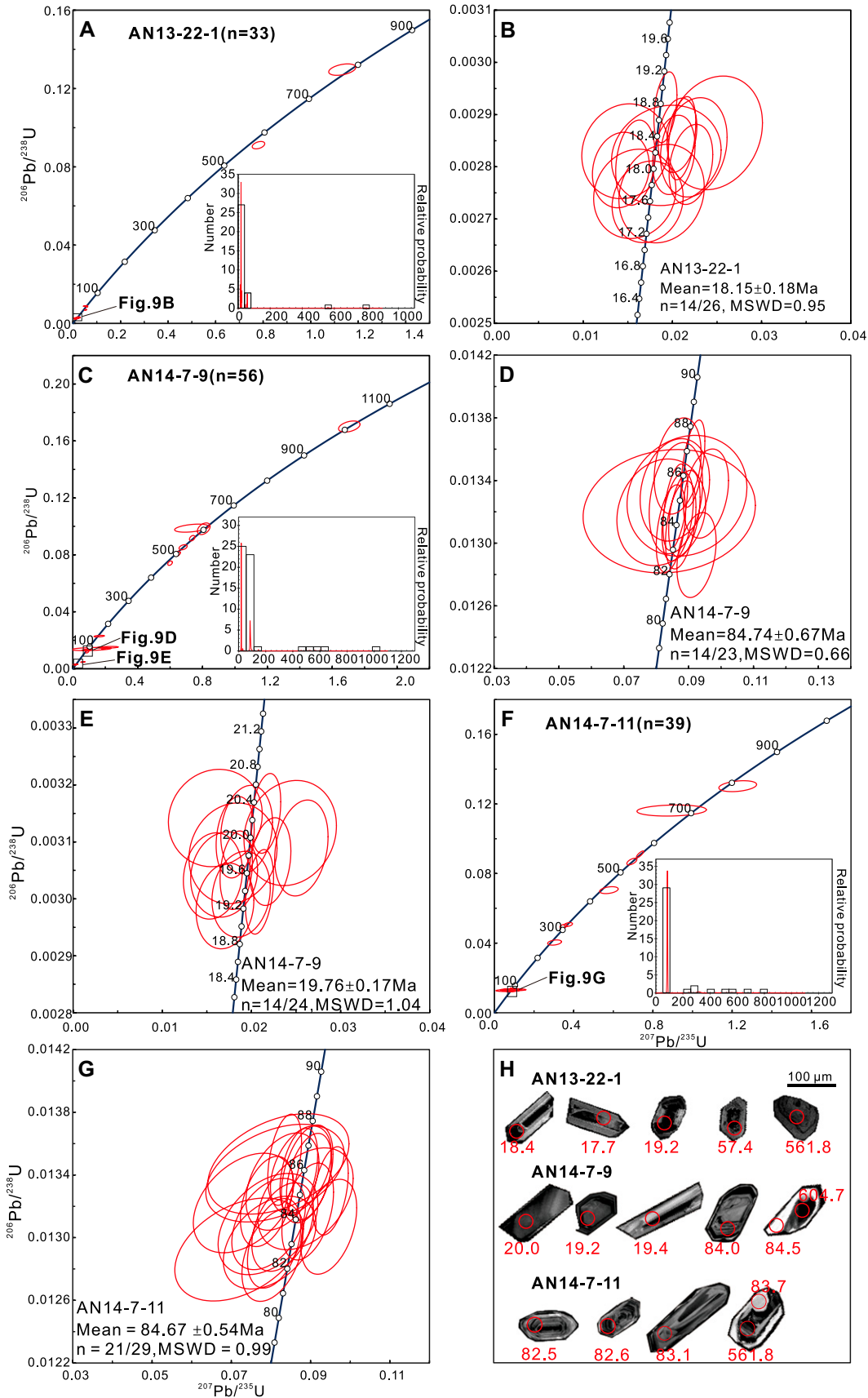
Figure 9. U-Pb concordia diagrams and representative cathodoluminescence (CL) images of zircon grains from regional Miocene volcanic rocks and the Angouran volcanic clasts-bearing breccias, northwestern Iran. (A and B) Concordia diagrams for the sample AN13-22-1 from regional Miocene volcanic rocks, ~500 m south of the Angouran open pit. (C–E) Concordia diagrams for the sample AN14-7-9 from the volcanic clasts-bearing breccias at Angouran. (F and G) Concordia diagrams for the sample AN14-7-11 from the volcanic clasts-bearing breccias at Angouran. (H) CL images of representative zircon grains. MSWD—mean square of weighted deviates; n—number of analysis.
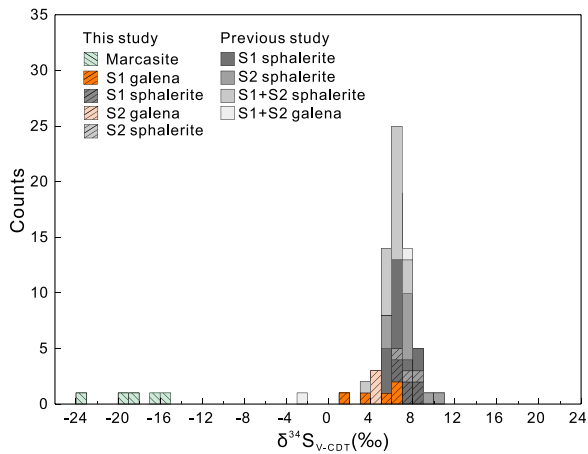
Figure 10. Sulfur isotope compositions of sulfides in the Angouran deposit, northwestern Iran. The analytical data are listed in Table S2 (see text footnote 1). Published data are collected from Gilg et al. (2006), Daliran et al. (2013), and Zhuang et al. (2019) and were determined by a conventional bulk analytic technique. S1—first stage; S2—second stage; V-CDT—Vienna-Canyon Diablo Troilite.

wall-rock schist (Fig. 12). Some of the quartz grains have extraordinarily high $\delta^{18}O$ values (up to 28.3‰). Such elevated $\delta^{18}O$ values are observed in quartz and chert pseudomorphs after sulfate in evaporitic environments where the $^{18}O$ enrichment is attributed to the influence of the sulfate phase and/or highly evaporated brine (Milliken, 1979; Henchiri and Slim-S'himi, 2006; Bustillo et al., 2017; Teboul et al., 2019). Tabular dolomite and spherical calcite inclusions are also identified in the double-terminated quartz (Figs. 8D and 8E). Such morphological carbonate mineral inclusions have only been reported for quartz precipitated from evaporitic environments in which the high Mg/Ca ratio prevents the axis-orientated growth of dolomite crystals (Perkins et al., 1994; Kovalevych et al., 2006; Sanz-Montero et al., 2006; Gillhaus et al., 2010). Experimental studies also indicate that the growth of spherical calcite (aragonite) requires high $SO_4^{2-}$ concentrations ($SO_4^{2-} \gg CO_3^{2-}$) in the aqueous solution (Fernández-Díaz et al., 2010; Bots et al., 2011). These observations and data suggest that the double-terminated quartz at Angouran precipitated from fluids in an evaporite environment. The quartz formed earlier than the sphalerite as it was corroded by S1 sphalerite (Figs. 8F and 8G). The quartz crystal growth from a breccia clast suggests that the double-terminated quartz deposition postdated the brecciation (Fig. 8C).

In summary, the salient features of the Angouran breccias are consistent with those of halokinetic diapir breccias, including the presence of (former) anhydrite and double-terminated quartz in a discordant breccia pipe with a dome structure, angular clasts, and mega-breccias, matrix-supported float breccias, flow textures, and exotic breccia clasts derived from the footwall unit (Kerr and Kopp, 1958; Jackson et al., 2003; Warren, 2016, and references therein; Leach et al., 2017; de Oliveira et al., 2019; Leach and Song, 2019). Evaporites from the basal URF may be responsible for the halokinesis in the Angouran deposit.

## Halokinetic Diapirism and Mineralization Process

The Angouran deposit has been classified as a sedimentary exhalative (SEDEX) deposit, a volcanogenic massive sulfide (VMS) deposit, a magmatic-related low-temperature deposit, and a Mississippi Valley-type (MVT) deposit (Maanijou, 2002; Daliran and Borg, 2005; Gilg et al., 2006; Daliran et al., 2013; Song et al., 2019; Zhuang et al., 2019). The hypothesis of a SEDEX or VMS deposit is unrealistic because the sulfide ores are hosted by a marble-schist sequence, which lacks a laminated or massive texture. The characteristics of the ore-forming fluids for the Angouran sulfide ores are consistent with MVT deposits (Gilg et al., 2006), and the trace elements in sphalerite are similar to MVT deposits and unlike magmatic-related deposits (Zhuang et al., 2019). Therefore, the Angouran deposit is best classified as a MVT deposit. The deposit is different from typical MVT deposits in that the ore-hosting rocks are metamorphic rocks but not carbonates. However, this is not weird because halokinetic diapir-related MVT mineralization can be hosted by a variety of rocks. For example, the world-class Jinding Zn-Pb deposit in southwestern China is hosted by sandstones and brecciated limestones (Leach et al., 2017; Leach and Song, 2019; Song et al., 2020).

The age determined for the volcanic rock clasts attests to a <19.76 ± 0.17 Ma post-brecciation event for the Angouran Zn-Pb mineralization. Gilg et al. (2006) suggested that the Miocene magmatism or the Plio-Pleistocene tectonic compression drove the flow of basinal brines to form the Angouran deposit. Given the mineralization is unrelated to magmatism, the Plio-

Pleistocene tectonic compression is more likely responsible for the Angouran Zn-Pb sulfide mineralization. The conceptual models for the halokinetic diapirs and the subsequent mineralization process are illustrated in Figure 13. The progressive NE-SW compression during Arabia-Eurasia continental collision since ca. 20 Ma resulted in the Precambrian–Cambrian metamorphic rocks being thrust over the Miocene evaporite-bearing volcanic-sedimentary sequences (Fig. 13A). The thrust loading probably triggered the halokinetic migration of Miocene evaporites along faults into the structurally overlying metamorphic sequence to form a discordant diapir breccia pipe containing breccia clasts that were derived mostly from country rocks and, to a lesser extent, from the rocks below (Figs. 13A and 13B).

Prior to Zn-Pb mineralization, trace amounts of pyrite and marcasite appear to have formed in the diapir via biogenetic sulfate reduction (BSR) in the presence of organic matter, as inferred from the extremely depleted $^{34}S$ composition (Fig. 10). Low-temperature BSR-related marcasite/pyrite deposition is a common process in evaporite diapir domes worldwide (Price and Kyle, 1983; Kyle and Posey, 1991; Sheppard et al., 1996). Organic matter is present along the thrust fault between the Neoproterozoic–Cambrian marble and the Miocene volcanic rocks, ~500 m south of the Angouran open pit (Fig. 2C; Daliran et al., 2013). Double-terminated quartz also likely formed during this period as a result of fluid circulation within the evaporite diapir.

Subsequent Zn-Pb sulfide mineralization was superimposed on the evaporites in the diapir likely during the Plio-Pleistocene tectonic compression (Time 2 in Fig. 13C). Most of the evaporites were replaced and dissolved before and/or during the mineralization, and two stages of sphalerite and galena precipitated by replacement of anhydrite and the filling of open spaces (Fig. 13C). The processes of replacement and filling are also common for sulfide mineralization within anhydrite-rich caprocks in evaporite domes worldwide and can form both euhedral anhydrite and anhydrite with irregular boundaries as observed in Angouran (Price et al., 1983; Ulrich et al., 1984; Kyle and Posey, 1991). Sulfur isotopes of the sphalerite and galena in Angouran (Fig. 10) allow a broad interpretation of reduced sulfur source(s), including thermo-chemical sulfate reduction (TSR) of marine sulfate by organic matter or by $Fe^{2+}$-rich mafic to ultramafic rocks, mixed magmatic and TSR-generated sulfur (Gilg et al., 2006; Daliran et al., 2013; Zhuang et al., 2019). Considering the presence of organic matter around the Angouran mineralization zone, the simplest interpretation is that reduced sulfur originated from the TSR process of the diapiric evaporite sulfates.
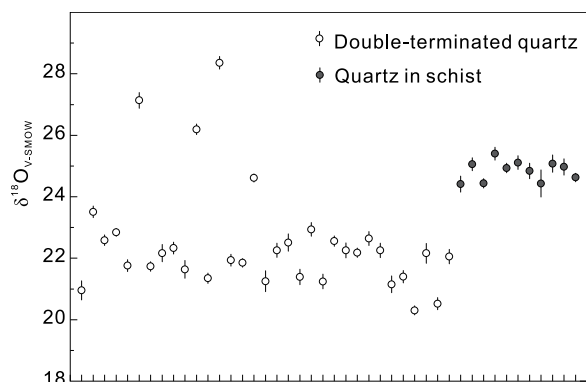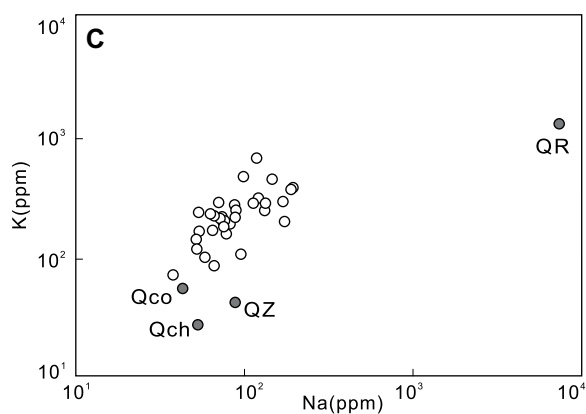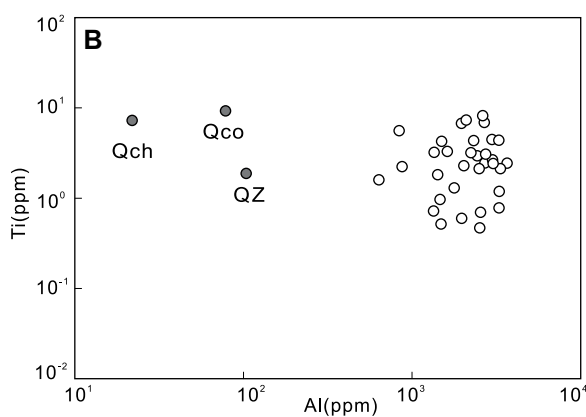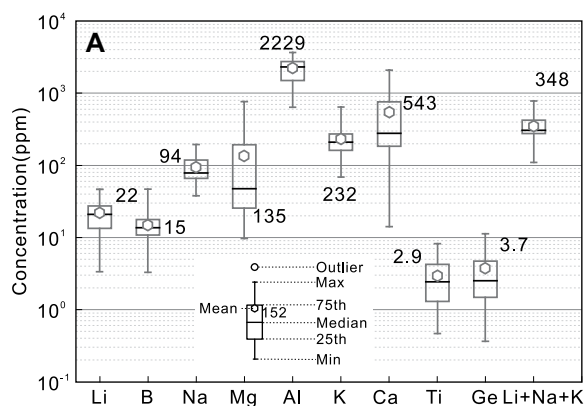
Figure 11. (A) Box diagram showing elemental concentrations in double-terminated quartz from the breccia matrix in the Angouran deposit, northwestern Iran. (B) Ti versus Al concentrations showing that the Angouran double-terminated quartz is characterized by high Al and low Ti. (C) K versus Na concentrations showing anomalously high K concentration in double-terminated quartz, compared to data from double-terminated quartz from the Permian (Zechstein) salt mines, central Europe. Data are given in Table S3 (see text footnote 1). Qch, Qco, QR, and QZ data are from Götze (2012). Qch—authigenic quartz from the Bunter sandstone; Qco—authigenic quartz from the Tertiary lignite, Conspuden, Germany; QR—authigenic quartz from the Zechstein salt deposits, Roßleben, Germany; QZ—authigenic quartz from the Tertiary lignite, Zwenkau, Germany.



Figure 12. The $\delta^{18}O_{V\text{-}SMOW}$ values of the double-terminated quartz from the sulfide ores and footwall schist, showing some of the double-terminated quartz grains have extraordinarily high $\delta^{18}O$ values. Analytical results are given in Table S4 (see text footnote 1). V-SMOW—Vienna standard mean ocean water.

Finally, in the middle to upper parts of the breccia pipe, supergene smithsonite overprinted the earlier sulfide mineralization (Time 3 in Fig. 13D). Smithsonite replaced sphalerite and possibly anhydrite, and filled the open spaces generated by the dissolution of these two minerals and marble clasts (Fig. 13D). A supergene model for the nonsulfide ore (Hirayama, 1986; Hitzman et al., 2003) was later modified by attributing part of the oxide mineralization to supergene processes, and/or a low-temperature hydrothermal alteration event (Daliran and Borg, 2005; Boni et al., 2007; Daliran et al., 2013).

## Identification of Halokinetic Structure with Vanished Evaporites and Its Implications for MVT Ore Formation and Exploration

Evaporite minerals, especially halite, are rapidly removed from the rock records by dissolution whereas gypsum or anhydrite can be diagenetically altered to carbonates by TSR or BSR processes, or replaced by barite, celestite, or silica during burial or hydrothermal processes (e.g., Warren, 2016, and references therein). When evaporites have been removed, halokinetic structures without evaporite minerals could easily be mistaken for tectonic, hydrothermal, or hydraulic fracturing (e.g., Ollier, 2007). Based on this study and previous reports, we summarize some characteristic features of halokinetic structures with minor or even without evaporite minerals including: (1) a large discordant breccia body that cuts different stratigraphic zones; (2) the breccia containing rock clasts from formations stratigraphically below the breccia; (3) breccia clasts being angular, chaotically oriented, and having a large range in diameters varying from centimeters to meters (megabreccia); (4) typically matrix-supported breccia with few clast to clast contacts; (5) flow-textured breccia showing clasts or matrix with a preferred orientation; and (6) occurrence of evaporite mineral pseudomorphs, anhydrite relics or meta-evaporites (e.g., albite, scapolite), and double-terminated quartz in the breccia matrix. These can be used to identify such halokinetic structures.

The formation of halokinetic breccia zones do not produce ore. Rather, they fundamentally influence the flow of fluids in the rock package. Perhaps the most important factor that controlled the ore is a dome that provided a trap for hydrocarbons and reduced sulfur from gypsum/anhydrite that provided a chemical trap for ascending metalliferous fluids. As shown in Angouran, Jinding, Daliangzi, and Tianbaoshan, these economically important MVT deposits are hosted within halokinetic diapirs that have commonly undergone strong dissolution and replacement before, during, and/or after Zn-Pb mineraliza-
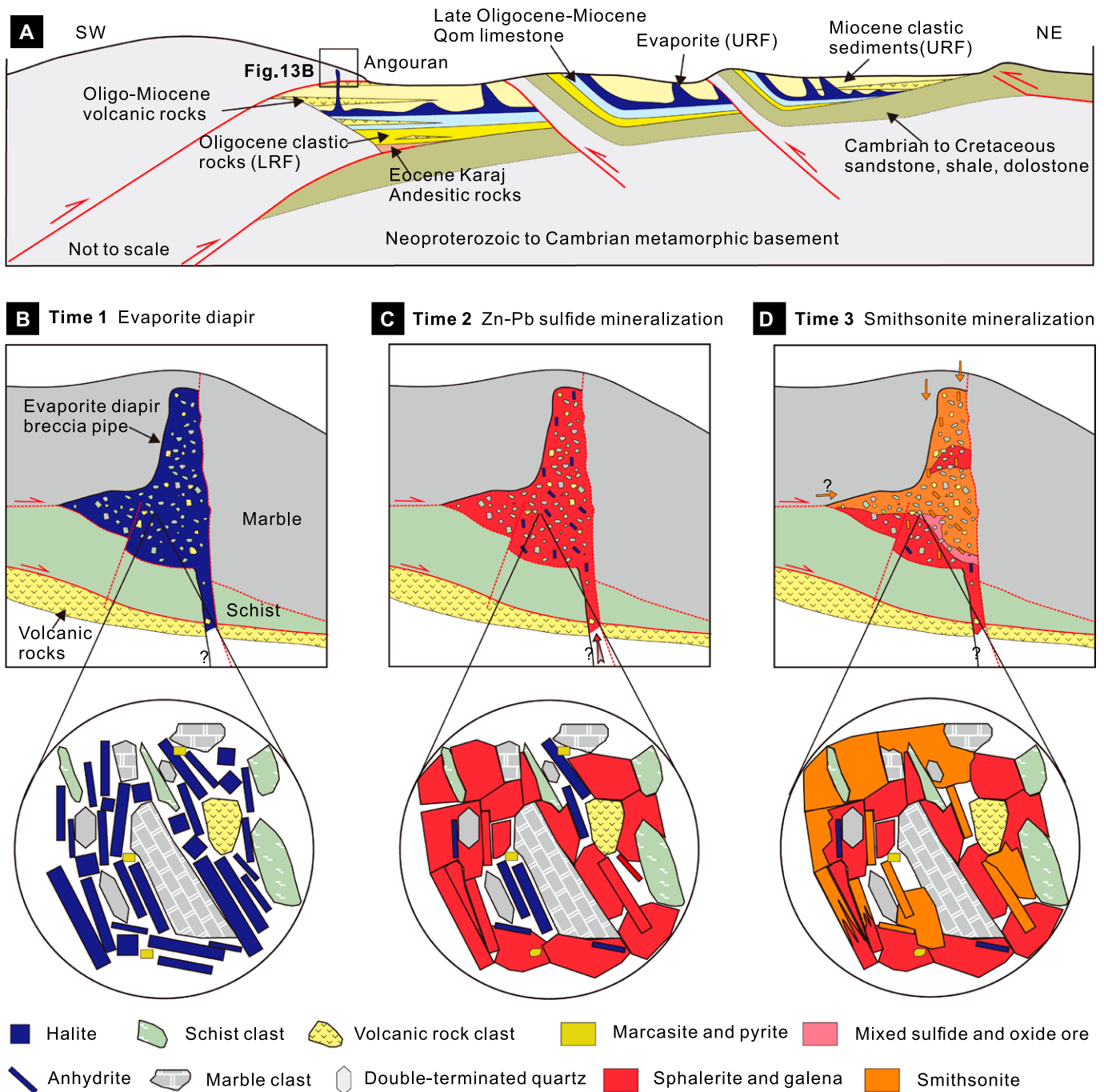
**Figure 13. A schematic diagram illustrating the evaporite diapir during regional tectonic evolution and mineralization events in the Angouran deposit, northwestern Iran. (A) The Neoproterozoic–Cambrian metamorphic basement thrusted onto the Miocene evaporate-bearing volcanic-volcaniclastic sequence during regional compression since late Miocene, and the halokinetic migration of Miocene evaporite into the Neoproterozoic–Cambrian metamorphic sequence. Basin architecture and regional structure were modified from Ballato et al. (2017). (B) Time 1: The evaporite diapir transported breccia clasts derived mostly from the country rocks (marble and schist) and subordinately from the Miocene volcanic rocks below. Double-terminated quartz may have formed in the diapir during this period. Trace amounts of marcasite and pyrite formed via biogenetic sulfate reduction. (C) Time 2: Zn-Pb sulfide mineralizing fluids migrated into the diapir where evaporite was mostly dissolved and replaced. Some sphalerite crystals are pseudomorphs after anhydrite as a result of the replacement, and less amounts of anhydrite were included in sphalerite crystals. Considering that sphalerite-hosted fluid inclusions are compositionally similar to a residual evaporated marine seawater with no obvious contribution of dissolving electrolytes from the evaporites (Gilg et al., 2006), the K- and Na-salts in the diapir could be largely dissolved before the Zn-Pb mineralization. (D) Time 3: Hypogene/supergene smithsonite mineralization was superimposed on the sulfide mineralization. Some smithsonite appears as "pseudomorphs after anhydrite," which are interpreted to be former sphalerite that replaced anhydrite crystals, or by infilling of cavities created by the dissolution of anhydrite. LRF—Lower Red Formation; URF—Upper Red Formation.**

tion (Leach et al., 2017; Song et al., 2017, 2019, 2020; Leach and Song, 2019). In contrast, the Tunisian examples suggest that if evaporites are well preserved in the evaporite diapirs, the halokinetic diapir bodies themselves have low permeability and thus contain few economic MVT Zn-Pb ores. In this case, ores usually occur in the peridiapiric rocks or transitional zones between diapirs and country rocks (Charef and Sheppard, 1987; Bouhlel et al., 2016; Rddad et al., 2019). The structures related to evaporite movement and modification must be considered in genetic and exploration models.

## CONCLUSIONS

The ore-hosting breccias at Angouran occur as a discordant pipe containing some volcanic rock clasts, with the absence of magmatic-related hydrothermal alterations. The consistent petrography and geochronology indicate that the volcanic rock clasts were derived from the underlying Miocene volcanic rocks. The matrix-supported float breccia clasts with a local flow texture give a chaotic appearance that is characteristic of diapirs. The anhydrite inclusions and abundant mineral pseudomorphs after anhydrite and double-terminated quartz with high concentrations of alkali earth elements and enrichment in heavy oxygen isotopes, as well as tabular and spherical carbonate inclusions trapped in these quartz crystals are further evidence that the breccia pipe was probably produced by halokinetic diapirism. The widespread occurrence of halokinesis for the Miocene evaporites in the Angouran region warrants this consideration. The bulk of the evaporite minerals were dissolved and replaced before and/or during Zn-Pb sulfide and later smithsonite mineralization events. Therefore, the breccia pipe originated as an evaporite diapir that became the host to the world-class Angouran sulfide and oxide ore deposit. Identification of a halokinetic structure with minor evaporates or without evaporites needs to consider the breccia structure, texture, component, and sources of clasts. The formation and modification of halokinetic structures can provide a permeable and chemical trap for ascending metalliferous fluids, causing ore deposition within the halokinetic breccia zones.

## REFERENCES CITED

Agard, P., Omrani, J., Jolivet, L., and Mouthereau, F., 2005, Convergence history across Zagros (Iran): Constraints from collisional and earlier deformation: International Journal of Earth Sciences, v. 94, p. 401–419, https://doi.org/10.1007/s00531-005-0481-4.

Agard, P., Omrani, J., Jolivet, L., Whitechurch, H., Vrielynck, B., Spakman, W., Monié, P., Meyer, B., and Wortel, R., 2011, Zagros orogeny: A subduction-dominated process: Geological Magazine, v. 148, p. 692–725, https://doi.org/10.1017/S001675681100046X.

Alavi, M., 1994, Tectonics of the Zagros orogenic belt of Iran: New data and interpretations: Tectonophysics, v. 229, p. 211–238, https://doi.org/10.1016/0040-1951(94)90030-2.

Alavi, M., and Amidi, M., 1976, Geological map of Takab quadrangle: Tehran, Geological Survey of Iran, scale 1:250,000.

Alireza, S., Jalal, D., and Mehran, M., 2007, Microfacies and sedimentary environments of the late Oligocene-early Miocene Qom Formation of the Gooreh Berenji region (Jandaq area, central Iran): GeoArabia, v. 12, p. 41–60, https://doi.org/10.2113/geoarabia120441.

Alizadeh, S., 2017, Non-diapiric salt domes in the West Zanjan, Central Iran: Open Journal of Geology, v. 7, no. 2, p. 132–146, https://doi.org/10.4236/ojg.2017.72009.

Allen, M.B., Kheirkhah, M., Emami, M.H., and Jones, S.J., 2011, Right-lateral shear across Iran and kinematic change in the Arabia-Eurasia collision zone: Geophysical Journal International, v. 184, p. 555–574, https://doi.org/10.1111/j.1365-246X.2010.04874.x.

Arian, M., 2012, Clustering of diapiric provinces in the Central Iran Basin: Carbonates and Evaporites, v. 27, p. 9–18, https://doi.org/10.1007/s13146-011-0079-9.

Azizi, H., Daneshvar, N., Mohammadi, A., Asahara, Y., Whattam, S.A., Tsuboi, M., and Minami, M., 2021, Early Miocene post-collision andesite in the Takab Area, NW Iran: Journal of Petrology, v. 62, https://doi.org/10.1093/petrology/egab022.

Ballato, P., Nowaczyk, N.R., Landgraf, A., Strecker, M.R., Friedrich, A., and Tabatabaei, S.H., 2008, Tectonic control on sedimentary facies pattern and sediment accumulation rates in the Miocene foreland basin of the southern Alborz mountains, northern Iran: Tectonics, v. 27, https://doi.org/10.1029/2008TC002278.

Ballato, P., Uba, C.E., Landgraf, A., Strecker, M.R., Sudo, M., Stockli, D.F., Friedrich, A., and Tabatabaei, S.H., 2011, Arabia-Eurasia continental collision: Insights from late Tertiary foreland-basin evolution in the Alborz Mountains, northern Iran: Geological Society of America Bulletin, v. 123, p. 106–131, https://doi.org/10.1130/B30091.1.

Ballato, P., Cifelli, F., Heidarzadeh, G., Ghassemi, M.R., Wickert, A.D., Hassanzadeh, J., Dupont-Nivet, G., Balling, P., Sudo, M., Zeilinger, G., Schmitt, A.K., Mattei, M., and Strecker, M., 2017, Tectono-sedimentary evolution of the northern Iranian Plateau: Insights from middle–late Miocene foreland-basin deposits: Basin Research, v. 29, p. 417–446, https://doi.org/10.1111/bre.12180.

Bao, Z., Chen, L., Zong, C., Yuan, H., Chen, K., and Dai, M., 2017, Development of pressed sulfide powder tablets for in situ sulfur and lead isotope measurement using LA-MC-ICP-MS: International Journal of Mass Spectrometry, v. 421, p. 255–262, https://doi.org/10.1016/j.ijms.2017.07.015.

Black, L.P., Kamo, S.L., Williams, I.S., Mundil, R., Davis, D.W., Korsch, R.J., and Foudoulis, C., 2003, The application of SHRIMP to Phanerozoic geochronology; a critical appraisal of four zircon standards: Chemical Geology, v. 200, p. 171–188, https://doi.org/10.1016/S0009-2541(03)00166-9.

Boni, M., Gilg, H.A., Balassone, G., Schneider, J., Allen, C.R., and Moore, F., 2007, Hypogene Zn carbonate ores in the Angouran deposit, NW Iran: Mineralium Deposita, v. 42, p. 799–820, https://doi.org/10.1007/s00126-007-0144-4.

Bots, P., Benning, L.G., Rickaby, R.E.M., and Shaw, S., 2011, The role of $SO_4$ in the switch from calcite to aragonite seas: Geology, v. 39, p. 331–334, https://doi.org/10.1130/G31619.1.

Bouhlel, S., Leach, D.L., Johnson, C.A., Marsh, E., Salmi-Laouar, S., and Banks, D.A., 2016, A salt diapir-related Mississippi Valley-type deposit: The Bou Jaber Pb-Zn-Ba-F deposit, Tunisia: Fluid inclusion and isotope study: Mineralium Deposita, v. 51, p. 749–780, https://doi.org/10.1007/s00126-015-0634-8.

Bustillo, M.A., Armenteros, I., and Huerta, P., 2017, Dolomitization, gypsum calcitization and silicification in carbonate-evaporite shallow lacustrine deposits: Sedimentology, v. 64, p. 1147–1172, https://doi.org/10.1111/sed.12345.

Chafetz, H.S., and Zhang, J., 1998, Authigenic euhedral megaquartz crystals in a Quaternary dolomite: Journal of Sedimentary Research, v. 68, p. 994–1000, https://doi.org/10.2110/jsr.68.994.

Charef, A., and Sheppard, S.M.F., 1987, Pb-Zn mineralization associated with diapirism: Fluid inclusion and stable isotope (H, C, O) evidence for the origin and evolution of the fluids at Fedj-El-Adoum, Tunisia: Chemical Geology, v. 61, p. 113–134, https://doi.org/10.1016/0009-2541(87)90032-5.

Chen, L., Chen, K., Bao, Z., Liang, P., Sun, T., and Yuan, H., 2017, Preparation of standards for in situ sulfur isotope measurement in sulfides using femtosecond laser ablation MC-ICP-MS: Journal of Analytical Atomic Spectrometry, v. 32, p. 107–116, https://doi.org/10.1039/C6JA00270F.

Chiu, H.Y., Chung, S.L., Zarrinkoub, M.H., Mohammadi, S.S., Khatib, M.M., and Iizuka, Y., 2013, Zircon U-Pb age constraints from Iran on the magmatic evolution related to Neotethyan subduction and Zagros orogeny: Lithos, v. 162–163, p. 70–87, https://doi.org/10.1016/j.lithos.2013.01.006.

Creaser, E.C., Steele-MacInnis, M., and Tutolo, B.M., 2022, A model for the solubility of anhydrite in $H_2O$-NaCl fluids from 25 to 800 °C, 0.1 to 1400 MPa, and 0 to 60 wt% NaCl: Applications to hydrothermal ore-forming systems: Chemical Geology, v. 587, https://doi.org/10.1016/j.chemgeo.2021.120609.

Daliran, F., and Borg, G., 2005, Characterisation of the non-sulphide zinc ore at Angouran, northwestern Iran, and its genetic aspects, in Mao, J., and Bierlein, F.P., eds., Mineral Deposit Research: Meeting the Global Challenge, Volume 2: Berlin, Germany, Springer, p. 913–916, https://doi.org/10.1007/3-540-27946-6_232.

Daliran, F., Borg, G., Armstrong, R., Walther, J., and Vennemann, T., 2009, Nonsulphide zinc deposits, Iran: The hypogene emplacement and supergene modification history of the Angouran zinc deposit, NW Iran: Hannover, Germany, BGR (German Federal Institute for Geosciences and Natural Resources), Berichte zur Lagerstätten und Rohstofforschung 57, 67 p.

Daliran, F., Pride, K., Walther, J., Berner, Z.A., and Bakker, R.J., 2013, The Angouran Zn (Pb) deposit, NW Iran: Evidence for a two stage, hypogene zinc sulfide-zinc carbonate mineralization: Ore Geology Reviews, v. 53, p. 373–402, https://doi.org/10.1016/j.oregeorev.2013.02.002.

de Oliveira, S.B., Leach, D.L., Juliani, C., Monteiro, L.V.S., and Johnson, C.A., 2019, The Zn-Pb mineralization of Florida Canyon, an evaporite-related Mississippi Valley-Type deposit in the Bongará district, Northern Peru: Economic Geology, v. 114, p. 1621–1647, https://doi.org/10.5382/econgeo.4690.

Fernández-Díaz, L., Fernández-González, Á., and Prieto, M., 2010, The role of sulfate groups in controlling $CaCO_3$ polymorphism: Geochimica et Cosmochimica Acta, v. 74, p. 6064–6076, https://doi.org/10.1016/j.gca.2010.08.010.

Friedman, G.M., and Shukla, V., 1980, Significance of authigenic quartz euhedra after sulfates; example from the Lockport Formation (Middle Silurian) of New York: Journal of Sedimentary Research, v. 50, p. 1299–1304.

Ghasemi, A., and Talbot, C.J., 2006, A new tectonic scenario for the Sanandaj-Sirjan Zone (Iran): Journal of Asian

Earth Sciences, v. 26, p. 683–693, https://doi.org/10.1016/j.jseaes.2005.01.003.

Gilg, H.A., Boni, M., Balassone, G., Allen, C.R., Banks, D., and Moore, F., 2006, Marble-hosted sulfide ores in the Angouran Zn-(Pb-Ag) deposit, NW Iran: Interaction of sedimentary brines with a metamorphic core complex: Mineralium Deposita, v. 41, p. 1–16, https://doi.org/10.1007/s00126-005-0035-5.

Gillhaus, A., Richter, D.K., Götte, T., and Neuser, R.D., 2010, From tabular to rhombohedral dolomite crystals in Zechstein 2 dolostones from Scharzfeld (SW Harz/Germany): A case study with combined CL and EBSD investigations: Sedimentary Geology, v. 228, p. 284–291, https://doi.org/10.1016/j.sedgeo.2010.05.003.

Götte, T., 2018, Trace element composition of authigenic quartz in sandstones and its correlation with fluid-rock interaction during diagenesis, *in* Armitage, P.J., Butcher, A.R., Churchill, J.M., Csoma, A.E., Hollis, C., Lander, R.H., Omma, J.E., and Worden, R.H., eds., Reservoir Quality of Clastic and Carbonate Rocks: Analysis, Modelling and Prediction: Geological Society, London, Special Publication 435, p. 373–387, https://doi.org/10.1144/SP435.2.

Götze, J., 2012, Mineralogy, geochemistry and cathodoluminescence of authigenic quartz from different sedimentary rocks, *in* Götze, J., and Möckel, R., eds., Quartz: Deposits, Mineralogy and Analytics: Berlin, Germany, Springer, p. 287–306, https://doi.org/10.1007/978-3-642-22161-3_13.

Götze, J., Plötze, M., Graupner, T., Hallbauer, D.K., and Bray, C.J., 2004, Trace element incorporation into quartz: A combined study by ICP-MS, electron spin resonance, cathodoluminescence, capillary ion analysis, and gas chromatography: Geochimica et Cosmochimica Acta, v. 68, p. 3741–3759, https://doi.org/10.1016/j.gca.2004.01.003.

Hassanzadeh, J., and Wernicke, B.P., 2016, The Neotethyan Sanandaj-Sirjan zone of Iran as an archetype for passive margin-arc transitions: Tectonics, v. 35, p. 586–621, https://doi.org/10.1002/2015TC003926.

Hassanzadeh, J., Stockli, D.F., Horton, B.K., Axen, G.J., Stockli, L.D., Grove, M., Schmitt, A.K., and Walker, J.D., 2008, U-Pb zircon geochronology of late Neoproterozoic–Early Cambrian granitoids in Iran: Implications for paleogeography, magmatism, and exhumation history of Iranian basement: Tectonophysics, v. 451, p. 71–96, https://doi.org/10.1016/j.tecto.2007.11.062.

Hearon, T.E., IV, Rowan, M.G., Lawton, T.F., Hannah, P.T., and Giles, K.A., 2015, Geology and tectonics of Neoproterozoic salt diapirs and salt sheets in the eastern Willouran Ranges, South Australia: Basin Research, v. 27, p. 183–207, https://doi.org/10.1111/bre.12067.

Heidari, S.M., Daliran, F., Paquette, J.L., and Gasquet, D., 2015, Geology, timing, and genesis of the high sulfidation Au (-Cu) deposit of Touzlar, NW Iran: Ore Geology Reviews, v. 65, p. 460–486, https://doi.org/10.1016/j.oregeorev.2014.05.013.

Henchiri, M., and Slim-S'himi, N., 2006, Silicification of sulphate evaporites and their carbonate replacements in Eocene marine sediments, Tunisia: Two diagenetic trends: Sedimentology, v. 53, p. 1135–1159, https://doi.org/10.1111/j.1365-3091.2006.00806.x.

Henchiri, M., Abidi, R., and Jemmali, N., 2015, Large euhedral quartz crystals in the Triassic dolomites and evaporites of central Tunisia: Implications for silica diagenesis in sulphate-rich and high-Mg environments: Arabian Journal of Geosciences, v. 8, p. 8899–8910, https://doi.org/10.1007/s12517-015-1788-5.

Hirayama, K., 1986, Geological Study on the Anguran Mine, Northwestern Part of Iran: Geological Survey of Japan Report 226, 25 p.

Hitzman, M.W., Reynolds, N.A., Sangster, D.F., Allen, C.R., and Carman, C.E., 2003, Classification, genesis, and exploration guides for nonsulfide zinc deposits: Economic Geology, v. 98, p. 685–714, https://doi.org/10.2113/gsecongeo.98.4.685.

Hitzman, M.W., Broughton, D., Selley, D., Woodhead, J., Wood, D., and Bull, S., 2012, The Central African Copperbelt: Diverse stratigraphic, structural, and temporal settings in the world's largest sedimentary copper district, *in* Hedenquist, J.W., Harris, M., and Camus, F., eds., Geology and Genesis of Major Copper Deposits

and Districts of the World: A Tribute to Richard H. Sillitoe: Society of Economic Geologists Special Publication 16, p. 487–514.

Honarmand, M., Xiao, W., Nabatian, G., Blades, M.L., dos Santos, M.C., Collins, A.S., and Ao, S., 2018, Zircon U-Pb-Hf isotopes, bulk-rock geochemistry and Sr-Nd-Pb isotopes from late Neoproterozoic basement in the Mahneshan area, NW Iran: Implications for Ediacaran active continental margin along the northern Gondwana and constraints on the late Oligocene crustal anatexis: Gondwana Research, v. 57, p. 48–76, https://doi.org/10.1016/j.gr.2017.12.009.

Hudec, M.R., and Jackson, M.P.A., 2007, Terra infirma: Understanding salt tectonics: Earth-Science Reviews, v. 82, p. 1–28, https://doi.org/10.1016/j.earscirev.2007.01.001.

Ickert, R.B., Hiess, J., Williams, I.S., Holden, P., Ireland, T.R., Lanc, P., and Clement, S.W., 2008, Determining high precision, in situ, oxygen isotope ratios with a SHRIMP II: Analyses of MPI-DING silicate-glass reference materials and zircon from contrasting granites: Chemical Geology, v. 257, p. 114–128, https://doi.org/10.1016/j.chemgeo.2008.08.024.

Jackson, M.P.A., and Hudec, M.R., 2017, Salt Tectonics: Principles and Practice: Cambridge, UK, Cambridge University Press, 498 p., https://doi.org/10.1017/9781139003988.

Jackson, M.P.A., Warin, O.N., Woad, G.M., and Hudec, M.R., 2003, Neoproterozoic allochthonous salt tectonics during the Lufilian orogeny in the Katangan Copperbelt, central Africa: Geological Society of America Bulletin, v. 115, p. 314–330, https://doi.org/10.1130/0016-7606(2003)115<0314:NASTDT>2.0.CO;2.

Jébrak, M., 1997, Hydrothermal breccias in vein-type deposits: A review of mechanisms, morphology and size distribution: Ore Geology Reviews, v. 12, p. 111–134, https://doi.org/10.1016/S0169-1368(97)00009-7.

Kerr, P.F., and Kopp, O.C., 1958, Salt-dome breccia: AAPG Bulletin, v. 42, p. 548–560.

Koshnaw, R.I., Stockli, D.F., and Schlunegger, F., 2019, Timing of the Arabia-Eurasia continental collision: Evidence from detrital zircon U-Pb geochronology of the Red Bed Series strata of the northwest Zagros hinterland, Kurdistan region of Iraq: Geology, v. 47, p. 47–50, https://doi.org/10.1130/G45499.1.

Kovalevych, V.M., Zang, W.L., Peryt, T.M., Khmelevska, O.V., Halas, S., Iwasinska-Budzyk, I., Boult, P.J., and Heithersay, P.S., 2006, Deposition and chemical composition of Early Cambrian salt in the eastern Officer Basin, South Australia: Australian Journal of Earth Sciences, v. 53, p. 577–593, https://doi.org/10.1080/08120090600686736.

Kuhn, T., Herzig, P.M., Hannington, M.D., Garbe-Schönberg, D., and Stoffers, P., 2003, Origin of fluids and anhydrite precipitation in the sediment-hosted Grimsey hydrothermal field north of Iceland: Chemical Geology, v. 202, p. 5–21, https://doi.org/10.1016/S0009-2541(03)00207-9.

Kyle, J.R., and Posey, H.H., 1991, Halokinesis, cap rock development, and salt dome mineral resources, *in* Mevlin, J.L., ed., Evaporites, Petroleum, and Mineral Resources: New York, USA, Elsevier, p. 413–474, https://doi.org/10.1016/S0070-4571(08)70263-2.

Kyle, J.R., and Saunders, J.A., 1996, Metallic deposits of the Gulf Coast basin: Diverse mineralization styles in a young sedimentary basin, *in* Sangster, D.F., ed., Carbonate-Hosted Lead-Zinc Deposits: 75th Anniversary Volume: Society of Economic Geologists Special Publication 4, p. 218–229.

Landtwing, M.R., and Pettke, T., 2005, Relationships between SEM-cathodoluminescence response and trace-element composition of hydrothermal vein quartz: The American Mineralogist, v. 90, p. 122–131, https://doi.org/10.2138/am.2005.1548.

Larsen, R.B., Henderson, I., Ihlen, P.M., and Jacamon, F., 2004, Distribution and petrogenetic behaviour of trace elements in granitic pegmatite quartz from South Norway: Contributions to Mineralogy and Petrology, v. 147, p. 615–628, https://doi.org/10.1007/s00410-004-0580-4.

Lawton, T.F., and Amato, J.M., 2017, U-Pb ages of igneous xenoliths in a salt diapir, La Popa basin: Implications

for salt age in onshore Mexico salt basins: Lithosphere, v. 9, p. 745–758, https://doi.org/10.1130/L658.1.

Leach, D., and Song, Y., 2019, Sediment-hosted zinc-lead and copper deposits in China, *in* Chang, Z., and Goldfarb, R.J., eds., Mineral Deposits of China: Society of Economic Geologists Special Publication 22, p. 325–349.

Leach, D.L., Song, Y.C., and Hou, Z.Q., 2017, The world-class Jinding Zn-Pb deposit: Ore formation in an evaporite dome, Lanping Basin, Yunnan, China: Mineralium Deposita, v. 52, p. 281–296, https://doi.org/10.1007/s00126-016-0668-6.

Lehmann, K., Pettke, T., and Ramseyer, K., 2011, Significance of trace elements in syntaxial quartz cement, Haushi Group sandstones, Sultanate of Oman: Chemical Geology, v. 280, p. 47–57, https://doi.org/10.1016/j.chemgeo.2010.10.013.

Leitner, C., Wiesmaier, S., Köster, M.H., Gilg, H.A., Finger, F., and Neubauer, F., 2017, Alpine halite-mudstone-polyhalite tectonite: Sedimentology and early diagenesis of evaporites in an ancient rift setting (Haselgebirge Formation, eastern Alps): Geological Society of America Bulletin, v. 129, p. 1537–1553, https://doi.org/10.1130/B31747.1.

Loucks, R.G., Mescher, P.K., and McMechan, G.A., 2004, Three-dimensional architecture of a coalesced, collapsed-paleocave system in the Lower Ordovician Ellenburger Group, central Texas: AAPG Bulletin, v. 88, p. 545–564, https://doi.org/10.1306/12220303072.

Ludwig, K.R., 2003, User's manual for Isoplot 3.00: A geochronological toolkit for Microsoft Excel: Berkeley Geochronology Center Special Publication 4, 74 p.

Maanijou, M., 2002, Proterozoic metallogeny of Iran: International Symposium on the Metallogeny of Precambrian Shields, Kiev, Russia, September 13–26, p. 13–26.

Maliva, R.G., 1987, Quartz geodes; early diagenetic silicified anhydrite nodules related to dolomitization: Journal of Sedimentary Research, v. 57, p. 1054–1059.

Marikos, M.A., 1989, Gangue anhydrite from the Viburnum Trend, southeast Missouri: Economic Geology, v. 84, p. 158–161, https://doi.org/10.2113/gsecongeo.84.1.158.

McQuarrie, N., and van Hinsbergen, D.J.J., 2013, Retrodeforming the Arabia-Eurasia collision zone: Age of collision versus magnitude of continental subduction: Geology, v. 41, p. 315–318, https://doi.org/10.1130/G33591.1.

Mehrabi, B., Yardley, B.W.D., and Cann, J.R., 1999, Sediment-hosted disseminated gold mineralisation at Zarshuran, NW Iran: Mineralium Deposita, v. 34, p. 673–696, https://doi.org/10.1007/s001260050227.

Milliken, K.L., 1979, The silicified evaporite syndrome; two aspects of silicification history of former evaporite nodules from southern Kentucky and northern Tennessee: Journal of Sedimentary Research, v. 49, p. 245–256.

Moazzen, M., Oberhänsli, R., Hajialioghli, R., Möller, A., Bousquet, R., Droop, G., and Jahangiri, A., 2009, Peak and post-peak P–T conditions and fluid composition for scapolite-clinopyroxene-garnet calc-silicate rocks from the Takab area, NW Iran: European Journal of Mineralogy, v. 21, p. 149–162, https://doi.org/10.1127/0935-1221/2009/0021-1887.

Moghadam, H.S., Griffin, W.L., Li, X.H., Santos, J.F., Karsli, O., Stern, R.J., Ghorbani, G., Gain, S., Murphy, R., and O'Reilly, S.Y., 2017, Crustal evolution of NW Iran: Cadomian arcs, Archean fragments and the Cenozoic magmatic flare-up: Journal of Petrology, v. 58, p. 2143–2190, https://doi.org/10.1093/petrology/egy005.

Morley, C.K., Kongwung, B., Julapour, A.A., Abdolghafourian, M., Hajian, M., Waples, D., Warren, J., Otterdoom, H., Srisuriyon, K., and Kazemi, M., 2009, Structural development of a major late Cenozoic basin and transpressional belt in central Iran: The Central Basin in the Qom-Saveh area: Geosphere, v. 5, p. 325–362, https://doi.org/10.1130/GES00223.1.

Mouthereau, F., Lacombe, O., and Vergés, J., 2012, Building the Zagros collisional orogen: Timing, strain distribution and the dynamics of Arabia/Eurasia plate convergence: Tectonophysics, v. 532–535, p. 27–60, https://doi.org/10.1016/j.tecto.2012.01.022.

Nadimi, A., and Nadimi, H., 2008, Exhumation of old rocks during the Zagros collision in the northwestern part of the Zagros Mountains, Iran, *in* Burchfiel, B.C., and

Wang, E., eds., Investigations into the Tectonics of the Tibetan Plateau: Geological Society of America Special Paper 444, p. 105–122, https://doi.org/10.1130/2008.2444(07).

Okamoto, A., and Tsuchiya, N., 2009, Velocity of vertical fluid ascent within vein-forming fractures: Geology, v. 37, p. 563–566, https://doi.org/10.1130/G25680A.1.

Ollier, C.D., 2007, Breccia-filled pipes: Distinguishing between volcanic and non-volcanic origins: Geografia Fisica e Dinamica Quaternaria, v. 30, p. 63–76.

Perkins, R.D., Dwyer, G.S., Rosoff, D.B., Fuller, J., Baker, P.A., and Lloyd, R.M., 1994, Salina sedimentation and diagenesis: West Caicos Island, British West Indies, *in* Purser, B., Tucker, M., and Zenger, D., eds., Dolomites: A Volume in Honour of Dolomieu: International Association of Sedimentologists Special Publication 21, p. 37–54.

Perona, J., Canals, À., and Cardellach, E., 2018, Zn-Pb mineralization associated with salt diapirs in the Basque-Cantabrian Basin, Northern Spain: Geology, geochemistry, and genetic model: Economic Geology, v. 113, p. 1133–1159, https://doi.org/10.5382/econgeo.2018.4584.

Posey, H.H., Kyle, J.R., and Agee, W.N., 1994, Relations between diapiric salt structures and metal concentrations, Gulf Coast sedimentary basin, southern North America, *in* Fontboté, L., and Boni, M., eds., Sediment-Hosted Zn-Pb Ores, Volume 10 of the Series Special Publication of the Society for Geology Applied to Mineral Deposits: Berlin, Germany, Springer, p. 139–164.

Price, P.E., and Kyle, J.R., 1983, Metallic sulfide deposits in Gulf coast salt dome cape rocks: Transactions-Gulf Coast Association of Geological Societies, v. 33, p. 189–193.

Price, P.E., Kyle, J.R., and Wessel, G.R., 1983, Salt dome related lead-zinc deposits, *in* Kisvarsanyi, G., Grant, S.K., Pratt, W.P., and Koenig, J.W., eds., International Conference on Mississippi Valley Type Lead-Zinc Deposits: Proceedings Volume: Rolla, Missouri, USA, University of Missouri–Rolla, p. 558–571.

Rahimpour-Bonab, H., and Kalantarzadeh, Z., 2005, Origin of secondary potash deposits; a case from Miocene evaporites of NW Central Iran: Journal of Asian Earth Sciences, v. 25, p. 157–166, https://doi.org/10.1016/j.jseaes.2004.02.004.

Rddad, L., Jemmali, N., Sośnicka, M., and Cousens, B., 2019, The genesis of the salt diapir-related Mississippi Valley-Type Ba-Pb-(± Zn) ore of the Slata district, Tunisia: The role of halokinesis, hydrocarbon migration, and Alpine orogenesis: Economic Geology, v. 114, p. 1599–1620, https://doi.org/10.5382/econgeo.4687.

Reuter, M., Piller, W.E., Harzhauser, M., Mandic, O., Berning, B., Rögl, F., Kroh, A., Aubry, M.P., Wielandt-Schuster, U., and Hamedani, A., 2009, The Oligo-/Miocene Qom Formation (Iran): Evidence for an early Burdigalian restriction of the Tethyan Seaway and closure of its Iranian gateways: International Journal of Earth Sciences, v. 98, p. 627–650, https://doi.org/10.1007/s00531-007-0269-9.

Rosa, D., Leach, D., Guarnieri, P., and Bekker, A., 2022, The Black Angel deposit, Greenland: A Paleoproterozoic evaporite-related Mississippi Valley-type Zn-Pb deposit: Mineralium Deposita, v. 58, p. 1–23.

Ross, P.S., Jébrak, M., and Walker, B.M., 2002, Discharge of hydrothermal fluids from a magma chamber and con-comitant formation of a stratified breccia zone at the Questa porphyry molybdenum deposit, New Mexico: Economic Geology, v. 97, p. 1679–1699, https://doi.org/10.2113/gsecongeo.97.8.1679.

Ruan, H.C., Hua, R.M., and Cox, D.P., 1991, Copper deposition by fluid mixing in deformed strata adjacent to a salt diapir, Dongchuan area, Yunnan Province, China: Economic Geology, v. 86, p. 1539–1545, https://doi.org/10.2113/gsecongeo.86.7.1539.

Rusk, B.G., Lowers, H.A., and Reed, M.H., 2008, Trace elements in hydrothermal quartz: Relationships to cathodoluminescent textures and insights into vein formation: Geology, v. 36, p. 547–550, https://doi.org/10.1130/G24580A.1.

Saki, A., 2010, Proto-Tethyan remnants in northwest Iran: Geochemistry of the gneisses and metapelitic rocks: Gondwana Research, v. 17, p. 704–714, https://doi.org/10.1016/j.gr.2009.08.008.

Sangster, D.F., 1988, Breccia-hosted lead-zinc deposits in carbonate rocks, *in* James, N.P., and Choquette, P.W., eds., Paleokarst: Heidelberg, Germany, Springer Verlag, p. 102–116, https://doi.org/10.1007/978-1-4612-3748-8_5.

Sanz-Montero, M.E., Rodríguez-Aranda, J.P., and Calvo, J.P., 2006, Mediation of endoevaporitic microbial communities in early replacement of gypsum by dolomite: A case study from Miocene lake deposits of the Madrid Basin, Spain: Journal of Sedimentary Research, v. 76, p. 1257–1266, https://doi.org/10.2110/jsr.2006.122.

Saunders, J.A., and Swann, C.T., 1994, Mineralogy and geochemistry of a cap-rock Zn-Pb-Sr-Ba occurrence at the Hazlehurst salt dome, Mississippi: Economic Geology, v. 89, p. 381–390, https://doi.org/10.2113/gsecongeo.89.2.381.

Sheppard, S.M.F., Charef, K., and Bouhlel, S., 1996, Diapirs and Zn-Pb mineralization: A general model based on Tunisian (N. Africa) and Gulf Coast (USA) deposits, *in* Sangster, D.F., ed., Carbonate-hosted lead-zinc deposits: 75th Anniversary Volume: Society of Economic Geologists Special Publication 4, p. 230–243.

Sillitoe, R.H., 2010, Porphyry copper systems: Economic Geology, v. 105, p. 3–41, https://doi.org/10.2113/gsecongeo.105.1.3.

Song, Y.C., Hou, Z., Liu, Y.C., and Zhang, H.R., 2017, Mississippi Valley-Type (MVT) Pb-Zn deposits in the Tethyan domain: A review: Geology in China, v. 44, p. 664–689 [in Chinese with English abstract].

Song, Y.C., Liu, Y.C., Hou, Z.Q., Fard, M., Zhang, H.R., and Zhuang, L.L., 2019, Sediment-hosted Pb-Zn deposits in the Tethyan domain from China to Iran: Characteristics, tectonic setting, and ore controls: Gondwana Research, v. 75, p. 249–281, https://doi.org/10.1016/j.gr.2019.05.005.

Song, Y., Hou, Z., Xue, C., and Huang, S., 2020, New mapping of the world-class Jinding Zn-Pb deposit, Lanping Basin, southwest China: Genesis of ore host rocks and records of hydrocarbon-rock interaction: Economic Geology, v. 115, p. 981–1002, https://doi.org/10.5382/econgeo.4721.

Stern, R.J., Anthony, E.Y., Ren, M., Lock, B.E., Norton, I., Kimura, J.I., Miyazaki, T., Hanyu, T., Chang, Q., and Hirahara, Y., 2011, Southern Louisiana salt dome xenoliths: First glimpse of Jurassic (ca. 160 Ma) Gulf of Mexico crust: Geology, v. 39, p. 315–318, https://doi.org/10.1130/G31635.1.

Stockli, D.F., Hassanzadeh, J., Stockli, L.D., Axen, G., Walker, J.D., and Dewane, T.J., 2004, Structural and geochronological evidence for Oligo-Miocene intra-arc low-angle detachment faulting in the Takab-Zanjan area, NW Iran: Geological Society of America Abstracts with Programs, v. 36, no. 5, p. 319.

Stöcklin, J., and Eftekharnezhad, J., 1969, Geological map of Zanjan quadrangle: Tehran, Geological Survey of Iran, scale 1:250,000.

Talbot, C.J., and Aftabi, P., 2004, Geology and models of salt extrusion at Qum Kuh, central Iran: Journal of the Geological Society, v. 161, p. 321–334, https://doi.org/10.1144/0016-764903-102.

Talbot, C.J., Farhadi, R., and Aftabi, P., 2009, Potash in salt extruded at Sar Pohl diapir, southern Iran: Ore Geology Reviews, v. 35, p. 352–366, https://doi.org/10.1016/j.oregeorev.2008.11.002.

Teboul, P.A., Durlet, C., Girard, J.P., Dubois, L., San Miguel, G., Virgone, A., Gaucher, E.C., and Camoin, G., 2019, Diversity and origin of quartz cements in continental carbonates: Example from the Lower Cretaceous rift deposits of the South Atlantic margin: Applied Geochemistry, v. 100, p. 22–41, https://doi.org/10.1016/j.apgeochem.2018.10.019.

Thomas, R., Ellison, R.A., Goodenough, K.M., Roberts, N.M.W., and Allen, P.A., 2015, Salt domes of the UAE and Oman: Probing eastern Arabia: Precambrian Research, v. 256, p. 1–16, https://doi.org/10.1016/j.precamres.2014.10.011.

Ulmer-Scholle, D.S., Scholle, P.A., and Brady, P.V., 1993, Silicification of evaporites in Permian (Guadalupian) back-reef carbonates of the Delaware Basin, West Texas and New Mexico: Journal of Sedimentary Research, v. 63, p. 955–965.

Ulrich, M.R., Kyle, J.R., and Price, P.E., 1984, Metallic sulphide deposits in the Winnfield Salt Dome, Louisiana: Evidence for episodic introduction of metalliferous brines during cap rock formation: Transactions-Gulf Coast Association of Geological Societies, v. 34, p. 435–442.

Warren, J.K., 2016, Evaporites: A Geological Compendium: Berlin, Germany, Springer, 1813 p., https://doi.org/10.1007/978-3-319-13512-0.

Williams, I.S., 1998, U-Th-Pb geochronology by ion microprobe, *in* McKibben, M.A., Shanks, W.C., III, and Ridley, W.I., eds., Applications of Microanalytical Techniques to Understanding Mineralizing Processes: Reviews in Economic Geology 7, p. 1–35.

Woodcock, N.H., and Mort, K., 2008, Classification of fault breccias and related fault rocks: Geological Magazine, v. 145, p. 435–440, https://doi.org/10.1017/S0016756808004883.

Zhuang, L., Song, Y., Liu, Y., Fard, M., and Hou, Z., 2019, Major and trace elements and sulfur isotopes in two stages of sphalerite from the world-class Angouran Zn-Pb deposit, Iran: Implications for mineralization conditions and type: Ore Geology Reviews, v. 109, p. 184–200, https://doi.org/10.1016/j.oregeorev.2019.04.009.